

# Contents

Abstract	12
<b>1 Introduction</b>	<b>12</b>
<b>2 Theoretical Background</b>	<b>13</b>
<b>3 Introduction</b>	<b>14</b>
3.1 Born-Oppenheimer Approximation . . . . .	16
3.2 Self-Consistent Mean-Field Theory . . . . .	16
3.3 Density Functional Theory . . . . .	17
3.3.1 Theory . . . . .	17
3.3.2 Solving the Kohn-Sham Equations . . . . .	19
3.3.3 Kohn-Sham Equations and Self-Consistency . . . . .	20
3.3.4 Practical steps towards accurate calculations . . . . .	20
3.3.5 Thomas-Fermi model . . . . .	20
3.3.6 Hohenburg and Kohn Theories . . . . .	20
3.4 From Density Functional Theory to Tight-Binding . . . . .	20
<b>4 Defects in Materials</b>	<b>21</b>
4.1 Vacancies and Solutes . . . . .	21
<b>5 Bibliography</b>	<b>21</b>
<b>6 Introduction (What, how, where, when, why?)</b>	<b>25</b>
<b>7 Fitting</b>	<b>25</b>
<b>8 sd fitting: Including hybridisation</b>	<b>27</b>
<b>9 Methods</b>	<b>29</b>
9.1 Rugg . . . . .	29
9.2 Chaari . . . . .	30
<b>10 What did each method find</b>	<b>32</b>
<b>11</b>	<b>32</b>
<b>12 Introduction</b>	<b>35</b>
<b>13 Computational Method</b>	<b>37</b>
13.1 Peierls Potential . . . . .	37
13.2 Preliminary calculations . . . . .	40

13.3	Fe-C binding energies . . . . .	41
13.4	Carbon concentration on dislocation line . . . . .	41
13.5	Line Tension Model . . . . .	42
13.5.1	Line-tension model in carbon environment . . . . .	43
13.5.2	Extension to more Fermi-Dirac statistics . . . . .	44
<b>14</b>	<b>Results</b>	<b>45</b>
14.1	Peierls Potential . . . . .	45
14.2	Preliminary calculations . . . . .	49
14.3	Fe-C binding energies . . . . .	50
14.4	Carbon concentration along on line . . . . .	55
14.5	Line Tension Model . . . . .	55
14.5.1	Prerequisites . . . . .	55
14.5.2	Kink-pair formation in pure iron . . . . .	58
14.5.3	Kink-pair formation enthalpy with a single carbon . . . . .	60
14.5.4	Kink-pair nucleation rate . . . . .	64
14.5.5	Kink-trapping . . . . .	66
14.6	Line-tension equilibrium conditions . . . . .	67
14.6.1	Dynamics of straight $1/2\langle 111 \rangle$ screw dislocation . . . . .	67
14.6.2	Dynamics of kink-pair formation in equilibrium . . . . .	69
14.7	Diffusion Barriers . . . . .	72
14.7.1	Theory . . . . .	72
14.7.2	Computational Method . . . . .	73
14.7.3	Enthalpies in dislocation movement with static carbon . . . . .	74
14.7.4	Modification of occupancies due to diffusion barrier . . . . .	76
<b>15</b>	<b>Discussion</b>	<b>78</b>
<b>16</b>	<b>Future work</b>	<b>79</b>
<b>17</b>	<b>Conclusion</b>	<b>80</b>
<b>18</b>	<b>Appendix</b>	<b>81</b>
18.1	Regularisation of interaction energy in quadrupolar array . . . . .	81
18.2	Zero-point energy calculation . . . . .	82
18.3	Smooth mapping of sites in equilibrium line-tension model . . . . .	82
<b>19</b>	<b>Bibliography</b>	<b>83</b>
<b>20</b>	<b>Regularisation of interaction energy in quadrupolar array</b>	<b>92</b>

## 21 Zero-point energy calculation

93

## 22 Smooth mapping of sites in equilibrium line-tension model 93

```
% Created 2021-09-02 Thu 15:46 % Intended LATEX compiler: pdfla-
tex [11pt]article [hyphens]url float [utf8]inputenc [T1]fontenc graphicx grf-
file longtable wrapfig rotating [normalem]ulem amsmath textcomp amssymb
capt-of hyperref [a4paper,12pt,oneside,print,numbered,index,PageStyleIII]Classes/PhDThesisPSnPDF
[left=37mm,right=30mm,top=35mm,bottom=30mm]geometry
libertine
longtable epigraph upgreek graphicx enumerate lipsum [font=small,labelfont=bf]caption
xr fixltx2e xfrac
amsmath
[format=hang]caption
float
subcaption
booktabs
amsfonts amsmath amssymb siunitx
00A0
[square, sort, numbers, authoryear]natbib
[backend=biber, style=numeric-comp, citestyle=numeric, sorting=nty,
natbib=true]biblatex [maxnames=5]
Department of Physics
```



King's College London

2022

```
% { % pdfauthor={Tigany Zarrouk}, % pdftitle={}, % pdfkeywords={},
% pdfsubject={}, % pdfcreator={Emacs 27.2 (Org mode 9.4)}, % pdflang={English}}
```

Tigany Noor Abubaker  
Tigany Zarrouk

Firstly I'd like to thank my supervisors, Prof. Mark Sansom for being continually helpful throughout this project. Also my other "nanopore" supervisors Prof. Hagan Bayley and Dr. Jayne Wallace.

To my family and friends, my parents who have always supported throughout my Oxford years. My friend Steph and fellow PhD-er, and also the "Welshies" whose ridiculousness has kept me laughing. Hilaritus - you know who you are. Also Jemma and Min - my fellow Oxford DPhil-ers for the whining.

Everyone who has helped me in the SBCB, David "**Blank Space**" Short-house, GB "**Red**" Morris, & Jo "**Fearless**" Lee. Also previous and past members such as Erin, Nat, Phill S, Phil F, Lukas, Greg, Maria, Rouse, Craig, Jerome and Syma for helping me throughout the many years I have been here.

Also to my internet distractions, be they Spotify, BBC Sport & Netflix for maintaining my sanity.

The following publications are mentioned in this thesis

- J. L. Trick, E. J. Wallace, H. Bayley and M. S. P. Sansom. "Designing a Hydrophobic Barrier within Biomimetic Nanopores," *ACS Nano*, vol 8, pp. 11268-11279, 2014.
- J. L. Trick, P. Aryal, S. Tucker and M. S. P. Sansom. "Molecular simulation studies of hydrophobic gating in nanopores and ion channels," *Biochemical Society Transactions*, vol 43, pp. 146-150, 2014.
- J. L. Trick, C. Song, E. J. Wallace, H. Bayley and M. S. P. Sansom. "Electrowetting of a Hydrophobic Gate: Computational Electrophysiology of Voltage-Gating in a Biomimetic Nanopore", *in prep*.
- J. L. Trick, E. J. Wallace, H. Bayley and M. S. P. Sansom. "Conformational State of the Ligand Gated Serotonin Receptor, A Simulation Study," *in prep*.

## Abstract

Molecular dynamics simulations are used to study the function of hydrophobic gates within models of biomimetic nanopores and in ligand-gated ion channels. A computational approach to building and simulating model  $\beta$ -barrel nanopores has been established to explore the effects of changing the shape and polarity of amino acids lining the pore lumen. Changing the position of such residues resulted in different water conductive states. In 14  $\beta$ -strand pores, a computationally transplanted hydrophobic barrier to water and ions has been demonstrated and characterised in detail using free energy calculations. Electrowetting of such a hydrophobic gate within a model  $\beta$ -barrel nanopore is demonstrated in simulation, using two different methods to apply a transmembrane electric field. An increase in the transmembrane voltage results in breakdown of the hydrophobic barrier, resulting in the flow of water and ions. The effect (electrowetting) is shown to be reversed upon the removal of the transmembrane voltage. An investigation into the possible hydrophobic gate of the 5-HT<sub>3</sub> receptor channel via free energy calculations and simulations confirmed that the crystal structure is in a closed conformation with respect to the flow of ions. This demonstrates that simulations and free energy calculations may be used to functionally annotate crystal structures of ion channels.

## List of Abbreviations

$\alpha$ HL	alpha-Hemolysin
ABF	adaptive biasing force
CG	coarse grained
c.o.m	centre of mass
DNA	deoxyribonucleic acid
dsDNA	double stranded DNA
ECD	extracellular domain
EM	electron microscopy
ENM	elastic network model
GNM	Gaussian network model
HG	hour glass
LGIC	ligand gated ion channel
LLL	STLLTS Nanopore
LJ	Lennard-Jones
N	number of $\beta$ strands
NLLN	STNLLNT nanopore
NLL	STNLLTS nanopore
NMR	nuclear magnetic resonance
MD	molecular dynamics
nAChR	nicotinic acetylcholine receptor
OMP	outer membrane protein
pLGIC	pentameric ligand gated ion channel
PBC	periodic boundary conditions
PME	particle mesh Ewald
PMF	potential of mean force
QM	quantum mechanics
$S$	shear
SCNT	silicon carbide nanotube
ssDNA	single stranded DNA
TM	transmembrane
TMD	transmembrane domain
VdW	Van der Waals
WHAM	weighted histogram analysis method
WT	wild type



# Contents

## List of Figures

1	Example code. . . . .	12
2	Diagram of DER location within a bearing and its characteristics, taken from [6]. (a) Axial and circumferential sections of a bearing inner ring. (b) Circumferential section of a bearing inner ring under optical microscope, where ferrite bands (white etching bands) are formed in the subsurface. (c) Diagram showing the structure of a WEB consisting of a ferrite band and a LC adjacent to it. One can see the DER region is composed of regions of ferrite interspersed in the parent martensite with lenticular carbides bordering the ferrite bands. . . . .	35
3	Schematics of dislocation simulation methods. Left: quadrupolar arrangement of dislocations in a simulation cell (grey square). This arrangement minimises the stress experienced by each dislocation in a periodic simulation. Cell vectors $\vec{U}_1$ and $\vec{U}_2$ are shown; $\vec{A}$ defines the cut plane between the dipoles. The dislocation positions, and their corresponding burger's vector direction, are denoted by the symbols $\otimes$ and $\odot$ , which are antiparallel to each other. Tilt components added to cell vectors to accomodate for the plastic strain are not shown. Right: cluster method, where atoms are displaced according the displacement field from the screw dislocation at the centre of the cluster, denoted by " $\S$ ". Atoms in the annulus $R_2 - R_1$ are fixed in position to the anisotropic elasticity solutions. Within $R_1$ , all atoms can relax. Periodicity is only imposed in the $Z$ direction. . . . .	38
4	Diagrams of dislocation core positions. "E", "H" and "S" correspond to the easy, hard and split core positions respectively. Left: core positions as seen along the $Z = \langle 111 \rangle$ direction, along the dislocation line. Atomic positions are shown as grey circles. Right: positions sampled within the triangle EHS used to determine the Peierls potential. . . . .	39

5	Comparison of 2d Peierls potentials of the $1/2\langle 111 \rangle$ screw dislocation between DFT [21] (top) and tight-binding ( <i>sd</i> non-orthogonal middle, canonical <i>d</i> , bottom). $x - y$ axes in units of $d = a\sqrt{2}/3$ . Energy scale is in meV. "E", "H" and "S" correspond to easy, hard and split core positions respectively, with the latter also corresponding to atomic positions. The relative energies between the different core positions is smaller in tight-binding compared to DFT. The split core as seen in tight-binding is reminiscent of EAM potentials, where the split core energy is lower than that of the hard core. The discrepancy is probably due to an insufficient repulsion at close range within the tight-binding model. . . . .	46
6	Left: Peierls barriers from atomistic calculations using canonical- <i>d</i> -band tight-binding, DFT and the Mendelev EAM potential, plots of the corresponding dislocation pathways can be found in figure 14. The EAM potential of Mendelev [?] has an unphysical well in the centre of the potential, while tight-binding and DFT produce single-humped potentials. Right: Peierls potential along the hard-split line. One can see in <i>s-d</i> tight-binding model pathway is similar in shape to the EAM potential of Mendelev [?]: it decreases consistently from the hard core to the split core. In DFT one finds a saddle point between the hard core and the midpoint. . . . .	48
7	Excess energy of dislocation clusters with differing radii for both the easy and hard core configurations. The prediction from elasticity theory is given by the black, dashed line. Deviation of both cores occur when cell size is small, creating an increase in the core energy, which elasticity theory cannot account for. . . . .	49
8	Initial (top) and final (bottom) positions and binding energies (eV) of carbon around the easy core. Binding energies are not shown for the initial positions. Top: initial positions before relaxation. Bottom: final positions and binding energies after relaxation. The core was constrained by fixing the top and bottom three atoms surrounding each of the cores. As shown by Ventelon [19], the first and second closest octahedral sites to the hard core decay to a prismatic position inside the hard core. . . . .	52

9	Initial (top) and final (bottom) positions and binding energies (eV) of carbon around the hard core. The core was constrained by fixing the three atoms surrounding each of the cores in the top and bottom layers. As shown by Ventelon [19], the first and second closest octahedral sites to the hard core decay to a prismatic position inside the hard core. . . . .	53
10	Variation of carbon concentration on the dislocation line $c_d$ for the highest-energy binding sites for the hard core (H1) and easy core (E2). Solid, dashed, dotted and dash-dotted lines correspond to dislocation densities of $1 \times 10^{12}$ , $1 \times 10^{14}$ , $1 \times 10^{15}$ and $5 \times 10^{15}$ respectively. The nominal carbon concentrations are 10, 100, 500 and 1000 appm from left to right, where around 1000 appm corresponds to the concentration of carbon at the solubility limit of C in ferrite: 0.02wt%. $c_d$ and $c_{\text{bulk}}$ reached self-consistency, with an absolute tolerance of $1 \times 10^{-6}$ . C-C interactions were taken into account with the repulsive first-neighbour interaction energy $V_{\text{CC}} = 0.30$ eV. No intersite interactions were taken into account. The maximum concentration of carbon around the easy core, drops off at a lower temperature than that of the hard core due to lower binding energy of the E2 site compared to the H1 site. The operating temperature is taken to be 50 deg C = 320 deg K. . . . .	56
11	Distance dependence of the binding energies of carbon to the $1/2\langle 111 \rangle$ screw dislocation in iron. Positive binding energies denote a favourable binding. . . . .	57
12	Parameterised distance dependence of carbon binding energies to the $1/2\langle 111 \rangle$ screw dislocation in iron. The sites chosen to fit to were determined by those sites a prismatic carbon in a hard core configuration would find itself, if the dislocation were to move without it along the $X = \langle \bar{2}11 \rangle$ direction. The triangle, labelled Hanlummyuang, refers to the binding energy resulting from measurement of the elastic dipole tensor from DFT calculations evaluated at 12 [33]. Binding energy of hydrogen to the $1/2\langle 111 \rangle$ screw dislocation also shown for comparison [20] . . . . .	57

13	Core positions of the line tension model from DFT (blue) and tight-binding (yellow) for the middle image corresponding the MEP and the kink-pair formation energy. Images were relaxed using the ODE String method of Makri and Ortner [27]. $P_x$ and $P_y$ correspond to the x/y-coordinate of the dislocation core position in each of the discretised layers of the dislocation. One finds that the kink width in tight-binding is wider than that found in DFT, which corresponds with the fact that the width is proportional to $b\sqrt{K/\Delta E_P}$ , where the reduction in $\Delta E_P^{\text{tbe}}$ is greater than the reduction in $K_{\text{tbe}}$ . . . . .	58
14	Comparison of minimum energy pathways from different atomistic calculations to the line-tension model. Dashed lines correspond to atomistic calculations. Solid lines are results from the line-tension models. Tight-binding follows a pathway much closer to that of DFT. EAM potentials predict that the dislocation core goes to the split core and then back to the easy core. Even though the Peierls landscape found in tight binding has similar characteristics to the EAM in terms of the energetic ordering of different core states, the description of the minimum energy pathway of the $1/2\langle 111 \rangle$ screw dislocation as it moves between core positions is in good agreement with DFT. . . . .	59
15	Comparison of $P_x$ lineshapes for the <i>sd</i> and <i>d</i> models in pure iron (top) and iron with a single carbon interacting with the central dislocation segment in E1 site (bottom). The highest enthalpy images, $H_{\text{max}}$ , for each of the models are shown in black. In pure iron, the <i>d</i> model lineshapes are offset from the <i>sd</i> due to the different Peierls potentials involved. With carbon along the path of migration, we find the dislocation intersects the solute, due to its large binding energy. . . . .	61
16	The migration path of the highest enthalpy images for both the <i>sd</i> and <i>d</i> tight-binding models with a single carbon in an E1 site. Carbon causes a deviation of the kink-pair formation path from the pure iron case (solid lines), due to carbon-dislocation binding. . . . .	62
17	Dependence of the kink-pair formation enthalpy with increasing stress on the $[111](\bar{1}\bar{1}0)$ direction. Solid lines: pure iron. Dotted lines: carbon ahead of the dislocation line in an octahedral site. Experimental data taken from Spitzig [34]. . . .	62

18	Enthalpies of straight screw dislocation in the line-tension model in an environment of carbon with concentrations determined by thermodynamical mean field model. Carbon concentration on the dislocation on the dislocation line is in equilibrium with the bulk according to the concentration given by the H1 site, where carbon is able to redistribute between the sites according to Maxwell-Boltzmann statistics. . . . .	68
19	Enthalpies of straight screw dislocation in the line-tension model in an environment of carbon with concentrations determined by thermodynamical mean field model. Concentration of carbon in each of the sites is fixed to its initial value, simulating the limit where carbon does not have time to equilibrate with dislocation movement. . . . .	68
20	Enthalpies of the maximum enthalpy images upon kink-pair formation with increasing carbon content. Carbon interaction causes a reduction in the enthalpy barrier as due to the negation of the effect of the bare Peierls potential. As the nominal carbon concentration passes 20 appm, the hard core is stabilised, thus causing the string method algorithm to find a global minimum closer to the hard core position. . . . .	69
21	Maximum enthalpy pathways found upon kink-pair formation in an environment of carbon for both tight-binding models at different nominal carbon concentrations. Concentrations shown are before the easy core becomes unstable. With an increase in carbon content, path starts to deviate towards the hard core. . . . .	70
22	$P_x$ lineshape comparison of differing concentrations of the canonical- $d$ tight-binding model. . . . .	70
23	Kink-pair formation enthalpy dependence on nominal carbon concentration without the application of stress. There is a consistent decrease in the mean kink-pair formation enthalpy with carbon content. . . . .	71
24	Positions of trap sites around dislocation segments upon kink-pair formation at a nominal carbon concentration of 30 appm. Path only shown to the hard core to demonstrate smooth mapping of trap sites going from easy to hard core. Equilibrium occupancies shown by coloured circles. . . . .	84

25	Positions of trap sites around dislocation segments upon kink-pair formation at a nominal carbon concentration of 30 appm. Path only shown to the hard core to demonstrate smooth mapping of trap sites going from easy to hard core. Equilibrium occupancies shown by coloured circles. . . . .	94
----	--	----

## List of Tables

2	Table of energies used to calculate the Peierls potential. All values in meV. $\Delta E_{\text{P}}^{\text{DFT}}$ values taken from [21]. . . . .	47
3	Decay relations between the initial and final sites upon relaxation of carbon interstitials around the hard core. . . . .	51
4	Table of energies leading to the zero-point energy corrected binding energy using the cluster method for simulation of dislocation-carbon interactions. <sup>a</sup> Tight-binding quadrupolar array results, starting from a fully relaxed easy core quadrupole extended to a depth of 3b with carbon introduced into the iH1 site in the middle layer, by both dislocations. <sup>b</sup> DFT results of Ventelon, using the same quadrupolar configuration as in <sup>a</sup> . In both quadrupolar simulations, carbon ended up in the H1 site. . . . .	54
5	Kink-pair formation energies between DFT, and the two flavours of tight-binding used with the line-tension model . . . . .	60
6	Peierls stress of screw dislocation taken from the line tension model with the effect of the correction to the Peierls stress from quantum effects, estimated by Proville [?]. DFT results are found from papers of Itakura and Krach [21, ?], where Itakura <i>et al.</i> used a DFT-derived line-tension model, and Kraych used DFT NEB calculations. * corresponds to use of Itakura DFT data in this implementation of the line-tension model. . . . .	64

7	Enhancement factors to the kink nucleation rate and corresponding critical temperatures. $c_d$ was taken as the value reached from self-consistency at $T=300K$ , at a dislocation density of $\rho = 10^{15}$ , as seen in figure 10. Kink-pair nucleation rate enhancements steadily increase until concentrations at which all dislocations are decorated with carbon, in the cases of $C_{nom} \geq 500$ appm. The critical temperatures are all well above operating temperature, so we can expect rate enhancements during operation. . . . .	65
8	Kink-pair nucleation rate in an environment of carbon using the results of the canonical $d$ -band model, using from equations (9) and (8) . . . . .	71

Introduction

## 1 Introduction

We can have equations and reference them using `eqref`, as seen in (1).

$$\omega_0 = \gamma B_0 \tag{1}$$

And we can have some code as well, as seen in code snippet ??.

```
(setq phd-thesis-status 'finishing)
```

Nullam eu ante vel est convallis dignissim. Fusce suscipit, wisi nec facilisis facilisis, est dui fermentum leo, quis tempor ligula erat quis odio. Nunc porta vulputate tellus. Nunc rutrum turpis sed pede. Sed bibendum. Aliquam posuere. Nunc aliquet, augue nec adipiscing interdum, lacus tellus malesuada massa, quis varius mi purus non odio. Pellentesque condimentum, magna ut suscipit hendrerit, ipsum augue ornare nulla, non luctus diam neque sit amet urna. Curabitur vulputate vestibulum lorem. Fusce sagittis, libero non molestie mollis, magna orci ultrices dolor, at vulputate neque nulla lacinia eros. Sed id ligula quis est convallis tempor. Curabitur lacinia pulvinar nibh. Nam a sapien.

Nullam eu ante vel est convallis dignissim. Fusce suscipit, wisi nec facilisis facilisis, est dui fermentum leo, quis tempor ligula erat quis odio. Nunc porta vulputate tellus. Nunc rutrum turpis sed pede. Sed bibendum. Aliquam posuere. Nunc aliquet, augue nec adipiscing interdum, lacus tellus malesuada massa, quis varius mi purus non odio. Pellentesque condimentum, magna ut suscipit hendrerit, ipsum augue ornare nulla, non luctus diam neque sit amet urna. Curabitur vulputate vestibulum lorem. Fusce sagittis, libero non molestie mollis, magna orci ultrices dolor, at vulputate neque nulla lacinia eros. Sed id ligula quis est convallis tempor. Curabitur lacinia pulvinar nibh. Nam a sapien.

Nullam eu ante vel est convallis dignissim. Fusce suscipit, wisi nec facilisis facilisis, est dui fermentum leo, quis tempor ligula erat quis odio. Nunc porta vulputate tellus. Nunc rutrum turpis sed pede. Sed bibendum. Aliquam posuere. Nunc aliquet, augue nec adipiscing interdum, lacus tellus malesuada massa, quis varius mi purus non odio. Pellentesque condimentum, magna ut suscipit hendrerit, ipsum augue ornare nulla, non luctus diam neque sit amet urna. Curabitur vulputate vestibulum lorem. Fusce sagittis, libero non molestie mollis, magna orci ultrices dolor, at vulputate neque nulla lacinia



eros. Sed id ligula quis est convallis tempor. Curabitur lacinia pulvinar nibh. Nam a sapien.

## 2 Theoretical Background

Nullam eu ante vel est convallis dignissim. Fusce suscipit, wisi nec facilisis facilisis, est dui fermentum leo, quis tempor ligula erat quis odio. Nunc porta vulputate tellus. Nunc rutrum turpis sed pede. Sed bibendum. Aliquam posuere. Nunc aliquet, augue nec adipiscing interdum, lacus tellus malesuada massa, quis varius mi purus non odio. Pellentesque condimentum, magna ut suscipit hendrerit, ipsum augue ornare nulla, non luctus diam neque sit amet urna. Curabitur vulputate vestibulum lorem. Fusce sagittis, libero non molestie mollis, magna orci ultrices dolor, at vulputate neque nulla lacinia eros. Sed id ligula quis est convallis tempor. Curabitur lacinia pulvinar nibh. Nam a sapien.

### 3 Introduction

To accurately model the behaviour of an assembly of atoms we must use quantum mechanics. The wavelength of electrons, as described by de Broglie  $\lambda = \hbar/p$ , is of comparable length to the atomic spacing in solids. The first postulate of quantum mechanics states that a quantum mechanical system can be described by a wavefunction, a function of the positions of the quantum mechanical entities, and time, which satisfies the Schrödinger wave equation. As such we know that the state of the system can be fully described by a *many body wavefunction*: a wavefunction which is a function of the positions of each of the electrons and nuclei in the system, which also depends on time.

Assuming that we have non-relativistic electrons, the Schrödinger equation one must solve is then

$$\left( \sum_i -\frac{1}{2} \nabla_i^2 + \frac{1}{2} \sum_i \sum_j \frac{1}{|\mathbf{r}_i - \mathbf{r}_j|} + \sum_i \sum_I \frac{-Z_I}{|\mathbf{r}_i - \mathbf{R}_I|} \right) \Psi(\{\mathbf{r}\}; t) = E \Psi(\{\mathbf{r}\}; t),$$

where  $\Psi(\{\mathbf{r}\}; t)$  is an eigenstate and Hartree units have been used ( $e = m = \hbar = 4\pi\epsilon_0 = 1$ ).

A time-independent observable is the expectation value of a given operator,

$$\hat{O} = \frac{\hat{O}\Psi}{\Psi\Psi},$$

this is an integral over all of the coordinates.

The electronic density operator is defined as

$$\hat{\rho}(\mathbf{r}) = \sum_{i=1}^N \delta(\mathbf{r} - \mathbf{r}_i)$$

$$\rho(\mathbf{r}) = \frac{\hat{n}(\mathbf{r})\Psi}{\Psi\Psi}.$$

The total energy is the expectation value of the Hamiltonian:

$$E = \frac{\hat{H}\Psi}{\Psi\Psi} \quad (2)$$

$$= \hat{T} + \hat{V}_{\text{int}} + \int d^3V_{\text{ext}}\rho(\mathbf{r}) + E_{II}, \quad (3)$$

where

$$V_{\text{ext}}(\mathbf{r}) = \sum_I -\frac{eZ_I}{|\mathbf{r} - \mathbf{R}_I|}$$

is the external potential due to the coulomb interaction between the electrons and the nuclei—the expectation value has been explicitly written as an integral over the local electron density,  $E_{II}$  is the classical electrostatic nucleus-nucleus interaction energy,  $V_{\text{int}}$  is the electron-electron interaction energy and  $\hat{T}$  is the expectation value of the electronic kinetic energy.

Stationary points in the total energy correspond to eigenstates of the many-body Hamiltonian. One can vary the ratio, or the numerator, in (3). The latter must be subjected to the constraint of orthonormality ( $\Psi\Psi = 1$ ), which is possible with the use of Lagrange multipliers. One finds that upon variation of the bra  $\Psi$  that the ket must satisfy the time-independent Schrödinger equation:

$$\hat{H}\Psi_m = E\Psi,$$

where  $\Psi_m$  is an eigenstate.

Quite often, the state we would most like to find is the lowest energy state (*ground state*) of the system, as this is the fundamental state from which other mechanisms return to or start from. This necessarily occurs at zero kelvin by the third law of thermodynamics. To find this state for the full system, one must minimise the energy with respect to the parameters of the many-body wavefunction that satisfies the Schrödinger equation and appropriate symmetry constraints (e.g. for electrons,  $\Psi$  must be antisymmetric). This quickly leads to an explosion of complexity: just describing wavefunction of the 22 electrons present in a single titanium, in a coarse  $10 \times 10 \times 10$  grid, one would need to tabulate  $(10^3)^{22} = 10^{66}$  complex numbers to describe the electronic wavefunction at each point in the grid. Clearly, minimising a function of this complexity is costly. To make the problem tractable, we must make a few approximations.

### 3.1 Born-Oppenheimer Approximation

The first impose an adiabatic approximation on the time-independent wavefunction, which allows us to separate nuclear and electronic motion: this is the Born-Oppenheimer approximation. One must first make the assumption that the wavefunction which describes the system is a product state between the nuclear and electronic portions of the system.

$$\psi(\mathbf{R}, \mathbf{r}) = \Phi(\mathbf{R}) \cdot \psi_{\mathbf{R}}(\mathbf{r}),$$

where  $\psi_{\mathbf{R}}(\mathbf{r})$  is the electronic wavefunction and  $\Phi(\mathbf{R})$  is the nuclear portion of the wavefunction.

Due to the large disparity in mass between an electron and the nucleus of an atom ( $M_{\text{Nuc}} \sim 2000m_e$ ) we can neglect the contribution to the Hamiltonian that comes from the nuclear kinetic energy operator acting on the electronic wavefunction.

$$T_{\text{Nuclear}}(\mathbf{R})\psi_{\mathbf{R}}(\mathbf{r}) = \sum_{I=1}^M -\frac{1}{2M_I} \nabla_{\mathbf{R}_I}^2 \psi_{\mathbf{R}}(\mathbf{r})$$

$$T_{\text{Electronic}}(\mathbf{r})\psi_{\mathbf{R}}(\mathbf{r}) = \sum_{i=1}^M -\frac{1}{2m_i} \nabla_{\mathbf{r}_i}^2 \psi_{\mathbf{R}}(\mathbf{r})$$

This results in the motion of the electrons being instantaneous with regard to the motion of the ions in the system: electrons relax into their ground state instantly with respect to any configuration of the ions. This results in the total energy being a function of only the nuclear coordinates [1].

To obtain the total energy, we can solve for the electronic part of the wavefunction and then solve for the nuclear wavefunction,

$$\left(T_{\text{Nuclear}} + E_{\mathbf{R}}\right)\Phi(\mathbf{R}) = E_{\text{Total}}\Phi(\mathbf{R}),$$

where  $E_{\mathbf{R}}$  contains all of the information of the configuration of the electrons in the system.

### 3.2 Self-Consistent Mean-Field Theory

A major development on the path to tractable calculations is that of Hartree and Hartree-Fock theory. A ansatz is made for the many-electron wavefunction, whereby we assume it is a product state between single particle orbitals:

$$\Psi(\{\mathbf{r}\}) = \phi(\mathbf{r}_1)\phi(\mathbf{r}_2) \dots \phi(\mathbf{r}_n).$$

Applying the variational principle to find the ground state,

$$\frac{\hat{H}\Psi}{\Psi\Psi} = 0$$

we obtain the Hartree equations.

Näively,

### 3.3 Density Functional Theory

#### 3.3.1 Theory

Now that the electronic motion has been decoupled from that of the nucleus, we can now try to find the ground-state solution for a given configuration of ions. A computationally tractable way of doing this for a many-body solid describing all of the electrons is via the *Density Functional Theory*.

Hohenburg and Kohn's seminal paper in 1964 proved that there exists an energy functional of the electron density which can provide the exact ground-state energy and density upon minimisation. This reduces the number of variables from  $3N$  to that of only 3 for any number of electrons  $N$  in the system of interest.

In 1965, Kohn and Sham then developed a formalism to practically calculate this ground-state density via a set of self-consistent equations: the Kohn-Sham equations.

The main tenet of Density Functional Theory is: given a system that consists of  $N$  electrons, there exists an energy functional of the local electron density  $E[\rho(\mathbf{r})]$ , which corresponds to an antisymmetric wavefunction  $\Psi$ ; upon minimisation by variation of the electron density, subject to the constraint that the number of electrons is conserved,

$$\int_{\text{all space}} \rho(\mathbf{r}) = N,$$

the resulting density is unique and the value of the functional is the ground-state energy. To obtain this result we can go through the following theory.

Assuming  $\rho(\mathbf{r})$  is the exact ground state density, and  $\Psi$  is the ground-state, by the variational principle we can write,

$$\Psi \hat{\mathcal{T}} + \frac{1}{2} \sum_i \sum_j \frac{1}{|\mathbf{r}_i - \mathbf{r}_j|} \Psi + \int \rho(\mathbf{r}) V_{\text{ext}}(\mathbf{r}) d\mathbf{r} \geq E_0.$$

The state  $\Psi$  may not be unique. To make it so, one can subject equation 3.3.1 to the constraints that the number of electrons is conserved and that  $\rho$  is constant.

This defines the functional:

$$F[\rho] = \min_{\Psi \rightarrow \rho} \Psi \hat{\mathcal{T}} + \frac{1}{2} \sum_i \sum_j \frac{1}{|\mathbf{r}_i - \mathbf{r}_j|} \Psi = T[\rho] + E_{ee}[\rho],$$

where the notation  $\Psi \rightarrow \rho$  is to show that the minimisation is with respect to all  $\Psi$  that can make the density  $\rho$ .

One can see the functional with the minimum value as the ground-state energy is then

$$E[\rho] = F[\rho] + E_{\text{ext}}[\rho],$$

where

$$E_{\text{ext}}[\rho] = E_{\text{ext}}[\rho(\mathbf{r})] = \int \rho(\mathbf{r}) V_{\text{ext}}(\mathbf{r}),$$

of which its functional derivative is  $V_{\text{ext}}$ .

By the Euler-Lagrange equations, one finds that the ground state must satisfy

$$\frac{\delta F[\rho]}{\delta \rho(\mathbf{r})} + V_{\text{ext}} = \mu.$$

A functional is an entity that maps a function to a value, similar as how a function maps a variable to a value. The Hohenburg-Kohn theorem states that there exists a functional of the electron density which has the correct ground state energy upon minimising the energy with respect to the electron density [2]. Thus all the information of the system is contained in the electron density, which reduces the minimisation problem from  $4M$  variables to one of just 3 for any number of electrons in the system.

To actually find this density, one can use the Kohn-Sham equations to find a self-consistent solution for the electron density [3].

To find the eigenvalues, one can replace the problem of solving a fully-interacting electronic system, with a given electronic density, by an auxiliary non-interacting electronic system which has the same electronic density. The resulting eigenvalues can be used to find the expectation value of the kinetic energy functional,  $T_s[\rho(\mathbf{r})]$ , which corresponds to the kinetic energy of the non-interacting (Kohn-Sham) system.

The Hohenburg-Kohn-Sham functional can be defined as

$$E_{\text{HKS}}[\rho] = T_s[\rho] + E_{\text{H}}[\rho] + E_{\text{xc}}[\rho] + E_{\text{ext}}[\rho] + E_{\text{ZZ}},$$

where  $T_s[\rho]$  is the kinetic energy of the fictitious non-interacting auxiliary system acting in the same effective potential  $V_{\text{eff}}[\rho]$ . The assumption made

here is that the ground state density of the non-interacting, auxiliary system is equal to that of the system with full electronic interactions.

This definition of the functional redefines the exchange-correlation functional: the difference between the true kinetic energy and that of the non-interacting system is added to it. Such that the true exchange-correlation functional has the form of

$$E_{\text{xc}}[\rho] = \left( \hat{T} - T_{\text{s}}[\rho] \right) + \left( \hat{V}_{\text{int}} - E_{\text{H}}[\rho] \right)$$

where we can interpret the first term as being the increase in kinetic energy from electronic correlation in a fully interacting system, compared to a non-interacting one—correlations cause electrons to move to more energetically favourable areas of the potential, thus increasing the kinetic energy—and the second term is difference in energy between a system with full electron-electron interactions ( $\hat{V}_{\text{int}} = \frac{1}{|\mathbf{r}-\mathbf{r}'|}$ ), which includes exchange and correlation effects, and the standard Hartree energy, which represents the energy from purely an electronic density, with no exchange-correlation.

The difference between the true kinetic energy  $\Delta T = T - T_{\text{s}}$  is now approximated by the exchange-correlation functional  $E_{\text{xc}}[\rho]$ . This is a reasonable approximation. Separating the kinetic energy from the long-range coulomb interactions means that the exchange-correlation potential can be approximated by an approximately local functional. Is this due the the fact that correlations basically lead to a screening of the coulomb potential?

### 3.3.2 Solving the Kohn-Sham Equations

The process by which this happens are as follows: one solves the Poisson equation for the Hartree potential, given an initial input density which on the first iteration is a sum of atom-centred charges, one finds the total effective potential for the system which is the sum of the Hartree potential, the potential from the nuclei ( $V_{\text{ext}}$ ) and the exchange-correlation potential  $V_{\text{xc}}$ . The Schrödinger equation is subsequently solved, and a new electron density is found. This density can be put back into the Poisson's equation to find the hartree potential and start the cycle again. These equations must be solved self-consistently as the electron density that one puts into Poisson's equation is the quantity that one solves for. Once the input and output densities are within some tolerance of each other, then one can say that the  $\rho^{\text{out}}(\mathbf{r}) = \rho^{\text{exact}}(\mathbf{r})$ , and the resulting Kohn-Sham eigenvalues are the ground state energies.

The Kohn-Sham eigenvalues are not strictly correct.

### 3.3.3 Kohn-Sham Equations and Self-Consistency

### 3.3.4 Practical steps towards accurate calculations

### 3.3.5 Thomas-Fermi model

### 3.3.6 Hohenburg and Kohn Theories

## 3.4 From Density Functional Theory to Tight-Binding

For a solution to the Kohn-Sham equations, one must have a self-consistent density: the input density, from which we construct the effective potential must be within some defined tolerance of the output density—constructed from the eigenvectors found upon diagonalisation of the hamiltonian.

One can apply perturbation theory to more closely understand the relationship between the input and output densities. We can expand the HKS functional, equation (3.3.1), to second order in deviations from the input density to obtain the second-order HKS functional:

$$\begin{aligned} E_{\text{HKS}}^{(2)}[\rho] = & \sum_{n \text{ occ}} f_n \hat{H}^{\text{in}} \psi_n \\ & - \int d\mathbf{r} \rho^{\text{in}}(\mathbf{r}) V_{\text{xc}}^{\text{in}}(\mathbf{r}) + E_{\text{xc}}[\rho^{\text{in}}] - E_{\text{H}}[\rho^{\text{in}}] + E_{\text{ZZ}} \\ & + \frac{1}{2} \int d\mathbf{r} \int d\mathbf{r}' \left\{ e^2 \frac{\delta\rho(\mathbf{r})\delta\rho(\mathbf{r}')}{|\mathbf{r} - \mathbf{r}'|} \right. \\ & \left. + \delta\rho(\mathbf{r}) \frac{\delta^2 E_{\text{xc}}}{\delta\rho(\mathbf{r})\delta\rho(\mathbf{r}')} \delta\rho(\mathbf{r}') \right\} \end{aligned}$$

where,  $\rho = \rho^{\text{in}} + \delta\rho$ . The first line represents the energy from the input hamiltonian, the second line subtracts the exchange-correlation energy from the first term, to encapsulate all exchange-correlation effects in the second term on the second line, the third term removes the Hartree contribution from the first line, which is a double-counting correction term, with the final term on the second line being the classical nucleus-nucleus interaction.

Omitting the final two lines in equation (??), we obtain the first-order functional, the Harris-Foulkes functional, where we remove the need for self-consistency in order to find the ground state energy. This is the basis for tight-binding.

Haydock, and Sutton *et al.*



## 4 Defects in Materials

### 4.1 Vacancies and Solutes

## 5 Bibliography

### References

- [1] M. W. Finnis, A. T. Paxton, M. Methfessel, and M. van Schilfgaarde, “Self-consistent tight-binding approximation including polarisable ions,” *MRS Proceedings*, vol. 491, jan 1997.
- [2] P. Hohenberg and W. Kohn, “Inhomogeneous electron gas,” *Phys. Rev.*, vol. 136, pp. B864–B871, Nov 1964.
- [3] W. Kohn and L. J. Sham, “Self-consistent equations including exchange and correlation effects,” *Phys. Rev.*, vol. 140, pp. A1133–A1138, Nov 1965.
- [4] V. Heine, “Electronic structure from the point of view of the local atomic environment,” in *Solid State Physics*, pp. 1–127, Elsevier, 1980.
- [5] A. T. Paxton and C. Elsässer, “Analysis of a carbon dimer bound to a vacancy in iron using density functional theory and a tight binding model,” *Physical Review B*, vol. 87, June 2013.
- [6] H. Fu, E. Galindo-Nava, and P. R.-D. del Castillo, “Modelling and characterisation of stress-induced carbide precipitation in bearing steels under rolling contact fatigue,” *Acta Materialia*, vol. 128, pp. 176–187, Apr. 2017.
- [7] A. H. King and J. L. O’Brian, *Microstructural Alterations in Rolling Contact Fatigue*, pp. 74–74–15. Advances in Electron Metallography: Vol. 6, ASTM International, nil.
- [8] A. B. Jones, *Metallographic Observations of Ball Bearing Fatigue Phenomena*, pp. 35–35–18. Symposium on Testing of Bearings, ASTM International, nil.
- [9] J. J. Bush, W. L. Grube, and G. H. Robinson, “Microstructural, microhardness and residual stress changes due to rolling contact,” *Tribology*, vol. 3, no. 4, p. 249, 1970.

- [10] H. Swahn, P. C. Becker, and O. Vingsbo, “Martensite decay during rolling contact fatigue in ball bearings,” *Metallurgical Transactions A*, vol. 7, pp. 1099–1110, Aug. 1976.
- [11] A. P. Voskamp and E. J. Mittemeijer, “State of residual stress induced by cyclic rolling contact loading,” *Materials Science and Technology*, vol. 13, no. 5, pp. 430–438, 1997.
- [12] I. Polonsky, “On white etching band formation in rolling bearings,” *Journal of the Mechanics and Physics of Solids*, vol. 43, no. 4, pp. 637–669, 1995.
- [13] H. Fu, W. Song, E. I. Galindo-Nava, and P. E. R.-D. del Castillo, “Strain-induced martensite decay in bearing steels under rolling contact fatigue: Modelling and atomic-scale characterisation,” *Acta Materialia*, vol. 139, no. nil, pp. 163–173, 2017.
- [14] A. Warhadpande, F. Sadeghi, and R. D. Evans, “Microstructural alterations in bearing steels under rolling contact fatigue part 1—historical overview,” *Tribology Transactions*, vol. 56, pp. 349–358, May 2013.
- [15] A. Warhadpande, F. Sadeghi, and R. D. Evans, “Microstructural alterations in bearing steels under rolling contact fatigue: Part 2—diffusion-based modeling approach,” *Tribology Transactions*, vol. 57, pp. 66–76, Nov. 2013.
- [16] A. P. Voskamp, R. Österlund, P. C. Becker, and O. Vingsbo, “Gradual changes in residual stress and microstructure during contact fatigue in ball bearings,” *Metals Technology*, vol. 7, no. 1, pp. 14–21, 1980.
- [17] S. Hashemi, “Strength-hardness statistical correlation in api x65 steel,” *Materials Science and Engineering: A*, vol. 528, no. 3, pp. 1648–1655, 2011.
- [18] H. K. D. H. Bhadeshia, “Solution to the bagaryatskii and isaichev ferrite–cementite orientation relationship problem,” *Materials Science and Technology*, vol. 34, pp. 1666–1668, May 2018.
- [19] L. Ventelon, B. Lüthi, E. Clouet, L. Proville, B. Legrand, D. Rodney, and F. Willaime, “Dislocation core reconstruction induced by carbon segregation in bcc iron,” *Physical Review B*, vol. 91, June 2015.

- [20] M. Itakura, H. Kaburaki, M. Yamaguchi, and T. Okita, “The effect of hydrogen atoms on the screw dislocation mobility in bcc iron: a first-principles study,” *Acta Materialia*, vol. 61, no. 18, pp. 6857–6867, 2013.
- [21] M. Itakura, H. Kaburaki, and M. Yamaguchi, “First-principles study on the mobility of screw dislocations in bcc iron,” *Acta Materialia*, vol. 60, pp. 3698–3710, May 2012.
- [22] E. Clouet, “Screw dislocation in zirconium: An ab initio study,” *Physical Review B - Condensed Matter and Materials Physics*, vol. 86, no. 14, pp. 1–11, 2012.
- [23] V. Bulatov, *Computer Simulations of Dislocations (Oxford Series on Materials Modelling)*. Oxford University Press, dec 2006.
- [24] E. Clouet, L. Ventelon, and F. Willaime, “Dislocation core energies and core fields from first principles,” *Physical Review Letters*, vol. 102, Feb. 2009.
- [25] S. Morito, J. Nishikawa, and T. Maki, “Dislocation density within lath martensite in fe-c and fe-ni alloys,” *ISIJ International*, vol. 43, no. 9, pp. 1475–1477, 2003.
- [26] D. Rodney and L. Provile, “Stress-dependent peierls potential: Influence on kink-pair activation,” *Physical Review B*, vol. 79, Mar. 2009.
- [27] S. Makri, C. Ortner, and J. R. Kermode, “A preconditioning scheme for minimum energy path finding methods,” *The Journal of Chemical Physics*, vol. 150, p. 094109, Mar. 2019.
- [28] G. A. Nematollahi, B. Grabowski, D. Raabe, and J. Neugebauer, “Multiscale description of carbon-supersaturated ferrite in severely drawn pearlitic wires,” *Acta Materialia*, vol. 111, pp. 321–334, June 2016.
- [29] R. Veiga, M. Perez, C. Becquart, E. Clouet, and C. Domain, “Comparison of atomistic and elasticity approaches for carbon diffusion near line defects in -iron,” *Acta Materialia*, vol. 59, pp. 6963–6974, Oct. 2011.
- [30] E. Simpson, *A Tight Binding Study of Dislocations in Iron and Their Interactions with Hydrogen*. PhD thesis, King’s College London, 2019.
- [31] E. Clouet, S. Garruchet, H. Nguyen, M. Perez, and C. S. Becquart, “Dislocation interaction with c in -fe: A comparison between atomic simulations and elasticity theory,” *Acta Materialia*, vol. 56, pp. 3450–3460, Aug. 2008.

- [32] C. Becquart, J. Raulot, G. Bencteux, C. Domain, M. Perez, S. Gar-ruchet, and H. Nguyen, “Atomistic modeling of an fe system with a small concentration of c,” *Computational Materials Science*, vol. 40, pp. 119–129, July 2007.
- [33] Y. Hanlummyuang, P. Gordon, T. Neeraj, and D. Chrzan, “Interactions between carbon solutes and dislocations in bcc iron,” *Acta Materialia*, vol. 58, pp. 5481–5490, Sept. 2010.
- [34] W. Spitzig and A. Keh, “Orientation dependence of the strain-rate sensitivity and thermally activated flow in iron single crystals,” *Acta Metallurgica*, vol. 18, p. 1021–1033, Sep 1970.
- [35] M. Finnis, *Interatomic Forces in Condensed Matter*. Oxford University Press.
- [36] H. Yoshinaga and S. Morozumi, “The solute atmosphere round a moving dislocation and its dragging stress,” vol. 23, no. 186, pp. 1367–1385.
- [37] B. Lüthi, F. Berthier, L. Ventelon, B. Legrand, D. Rodney, and F. Willaime, “Ab initio thermodynamics of carbon segregation on dislocation cores in bcc iron,” *Modelling and Simulation in Materials Science and Engineering*, vol. 27, p. 074002, July 2019.
- [38] P. Maugis and D. Kandaskalov, “Revisiting the pressure effect on carbon migration in iron,” *Materials Letters*, vol. 270, p. 127725, July 2020.
- [39] W. Cai, V. V. Bulatov, J. Chang, J. Li, and S. Yip, “Periodic image effects in dislocation modelling,” *Philosophical Magazine*, vol. 83, pp. 539–567, Jan. 2003.

## 6 Introduction (What, how, where, when, why?)

Fitted canonical d titanium model such that we could have a better description of titanium within a tight-binding framework. Empirical potential are not accurate enough to describe the intricacies of the titanium structure.

## 7 Fitting

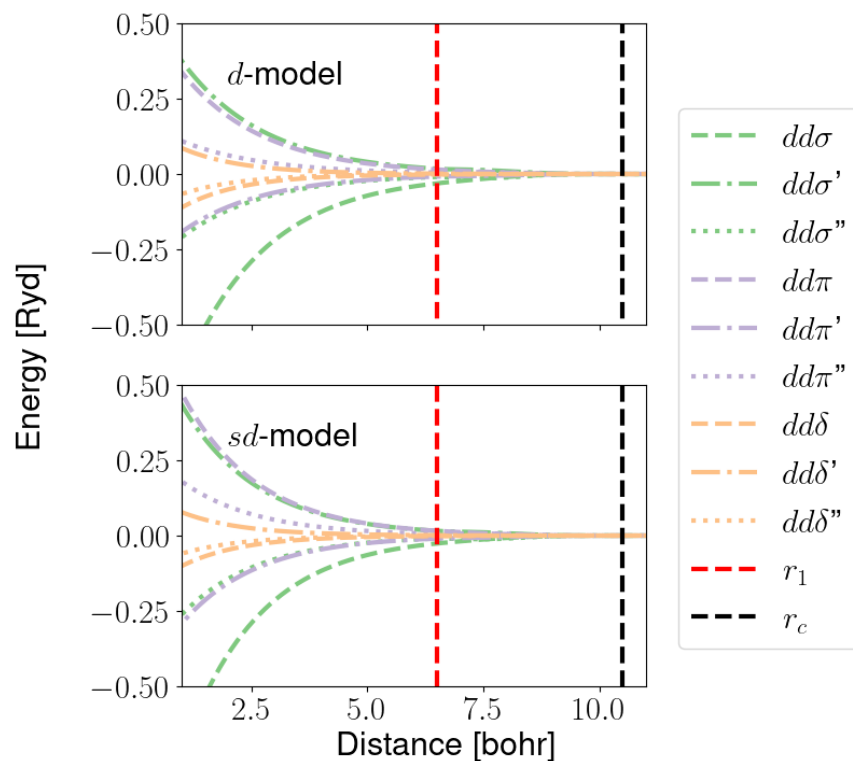
The overlap integrals were chosen to have a simple exponential distance dependence, as initially formulated by Ducastelle, [?] and Allan [?]. This form was originally motivated by an approximation to the density of states, of which the form was taken to be a Gaussian fitted to the second-moment of the distribution [?]. Analysis of the hybridisation of  $d$  states with nearly-free electron states in transition metals gives rise to  $d$ -band resonances, which suggest a fifth-degree power law distance dependence of  $d$ -orbitals for the matrix elements [?, 4, ?, ?, ?]. However, it has not been shown that a power-law dependence exhibits better transferability over a simple exponential dependence [?, ?]. Many power-law models have not fared well in predicting data outside of their fitting range [?, ?, ?, ?, ?]. Furthermore, exponentials do not have large first or second derivatives compared to power laws when modified by the cutoff function, which complicates fitting for elastic properties, and would provide erroneous forces [?]. Transferability has been consistently shown for the iron tight-binding model created by Paxton and Elsässer [?], which a more flexible exponential dependence. Their model predicts data well outside of their fitting range: non-degenerate dislocation core structures found in the bcc phase [?, ?], phonons and vacancy-formation energies. In addition, the Fe-Fe interactions have been shown suitable when incorporated with Fe-H/Fe-C interactions, to describe of hydrides and carbides [?, 5].

The bond integrals and pair potential ranges were chosen to start decaying to zero by a multiplicative polynomial between first and second neighbours in the hcp structure, going to zero between the second and third-neighbours. It was verified that the cutoffs were not close to neighbour shells found in titanium polymorphs, such that in future simulations, there would be no large and sudden forces arising from the inclusion of extra neighbours upon deformation. A multiplicative cutoff type was preferred over augmentative as it has been shown mitigate the effect of large second-derivatives,

which would cause difficulty in replicating experimental elastic constants and phonon dispersion [?].

In fitting, it was found that having only first-neighbour interactions, did not give desirable properties for the hcp phase: elastic constants which resulted in negative Cauchy pressures and a poor description of the energy difference between titanium polymorphs. Increasing the range of the interactions to second-neighbours resulted in more favourable results.

The form of the pair potential was chosen to be simple sum of two exponentials and a rapidly decaying power law term. The exponentials, which have one large positive term, and a smaller negative term, contribute the most over the range of interaction, with the power law chosen to only increase the repulsion at smaller distances. The addition of this power law gave more desirable gamma surface energies more reminiscent of DFT. This will be discussed in section **SECTION LABEL**. The resultant pair potential was highly repulsive at short distances, yet became slightly attractive at larger distances. This allowed for one to approximately account for attractive effect of  $s - d$  hybridisation in this simple  $d$ -orbital only model, as done in previous exclusively  $d$ -orbital tight-binding models for titanium [?]. Even though hybridisation is not strictly pairwise in character, we did not deem it necessary at this time to complicate matters further.



## 8 sd fitting: Including hybridisation

We included s orbitals such that one could more readily model the  $\text{Ti}^{4+}$  oxidation state of the Ti ion, which would give a more physical representation of titanium ions in quantum electrochemistry calculations.

Quantity	$d$ model	$s - d$ model	Target
a <sub>hcp</sub>	5.58523112		5.57678969
c/a	1.58371266		1.58731122
a <sub>omega</sub>	8.93475285		8.73254342
c <sub>omega</sub>	5.38726911		5.32343103
a <sub>4h</sub>	5.57584691		5.56325146
c <sub>4h</sub>	18.09810672		17.75908031
a <sub>6h</sub>	5.57365569		5.54639384
c <sub>6h</sub>	27.18378460		26.77136353
a <sub>bcc</sub>	6.20079768		6.17948863
a <sub>fcc</sub>	7.87290654		7.88677000
DE(o,h)	0.58764167		-0.63343333
DE(4h,h)	1.58019500		3.17160000
DE(6h,h)	2.48264833		3.72005000
DE(b,h)	5.35128500		7.63520000
DE(f,h)	3.78088500		4.51880000
c <sub>11</sub>	171.60928873		176.10000000
c <sub>33</sub>	198.90063708		190.50000000
c <sub>44</sub>	47.42549704		50.80000000
c <sub>12</sub>	94.65941969		86.90000000
c <sub>13</sub>	61.22624060		68.30000000
M <sub>freq0</sub>	2.59341377		2.85858719
M <sub>freq1</sub>	2.59341378		2.85858719
M <sub>freq2</sub>	2.59341378		2.85858719
M <sub>freq3</sub>	2.59341379		2.85858719
M <sub>freq4</sub>	5.85272461		5.66706047
M <sub>freq5</sub>	5.85272461		5.66706047
H <sub>freq0</sub>	3.82320403		4.80643423
H <sub>freq1</sub>	3.82320403		5.58010025
H <sub>freq2</sub>	6.40288977		5.65316738
H <sub>freq3</sub>	6.40288977		6.36651842
H <sub>freq4</sub>	7.92857431		6.40050186
H <sub>freq5</sub>	7.92857431		7.64082373
bandw. G	3.69394702		5.87085872
bandw. K	4.65178817		4.97424321
bandw. M	5.19329495		7.78109872
bandw. L	4.21232412		6.34433701
bandw. H	3.54700549		9.70902614
DOS <sub>serr<sub>h</sub></sub>	0.00000000		0.00000000
DOS <sub>serr<sub>o</sub></sub>	0.00000000		0.00000000
E <sub>prisf</sub>	98.95340236		220.00000000



## 9 Methods

### 9.1 Rugg

Theoretical analysis showed

Solute-dislocation interactions arise from two primary mechanisms: elastic interactions mediated by the long-ranged strain fields produced by a dislocation, and shorter-ranged interactions with the dislocation core that are generally referred to as “chemical” interactions (4, 6). The former are generally weak (on the scale of  $\sim 0.1$  eV per solute atom); in fact, symmetry constraints have the consequence that there should be no linear elastic interaction at all between oxygen interstitials at octahedral sites and a straight  $\langle a \rangle$  screw dislocation in the hcp structure. Analysis is found in the supplementary material.

Short range interactions can change the restoring force of the dislocation due to lattice slip. Which can be described by the gamma surface energy.

Two paths:

- I = octahedral site in perfect lattice
- II = Newly formed octahedral site formed by slip of  $0.5a$
- If oxygen on path of the slip plane (prismatic, I assume)
  1. GSF energy is much higher than for pure Ti
  2. Original octahedral site gradually disappears and transforms to a tetrahedral site with a lower interstitial volume, when the magnitude of the slip is  $0.5a$ .
  3. Concurrently, a new octahedral site is formed on the basal plane of the Ti structure.
  4. Changing from the tetrahedral to the new octahedral site reduces the energy by as much as 1.6 eV.
  5. These results give a barrier for oxygen shuffle (hopping) from path I to path II varies between 0.45-0.95eV, depending on magnitude of slip displacement, which gives a large diffusion barrier.
  6. Large increase in energy coupled with the large diffusion barrier means that the oxygen cannot move and thus there are strengthening effects.

7. The volume changes can be correlated with changes in interstitial volume upon dislocation slip.
8. The most pronounced volume changes occur on the prismatic slip plane, where the core structure of the dislocation is spread.
9. Interaction energies are apparently quite weak ( $\sim 60\text{meV}$  on neighbouring prismatic planes to the dislocation spread) or a distance larger than  $c/2$  on the prismatic plane of the dislocation spread.
10. With oxygen in the vicinity of the dislocation core there is a strong repulsive interaction which causes the dislocation to cross slip onto an adjacent prismatic plane.
11. If oxygen is on the basal plane (path II) then there is only a small repulsive interaction ( $-50\text{meV}$ ).

So arguments summarised as follows:

1. As evidenced by oxygen being found on basal planes in lightly deformed samples, due to the slip of a dislocation deforming the octahedral site into one of a smaller interstitial volume, oxygen will change site to an octahedral void on the basal plane of the dislocation, where the oxygen will remain 'stuck'.
2. Cross-slip of the dislocation may occur onto another prismatic plane. This will generate edge segments which connect the two screw dislocations in each of their planes. These edge segments can only move on the basal planes perpendicular to the prismatic planes. Due to the high GSF energy, their mobility is limited.
3. The resolved shear stress to move these edge segments is zero if one were to apply stress to cause the dislocation to move on the prismatic plane. This effectively causes a pinning effect of the oxygen near the dislocation core, providing a mechanism for oxygen solute strengthening.

## 9.2 Chaari

- Know that dislocation, in plane wave codes, seems to have a ground state in the first order pyramidal plane and to move it must change into a metastable state dissociated on the prismatic plane to glide easily. This is the locking-unlocking mechanism of Rodney.

- Extend work of Rugg to see how oxygen can change the transitions between core states which allow for glide.
- Main results are
  1. When the oxygen is placed in an octahedral site which is destroyed upon dissociation of the dislocation into partials on either the ground-state pyramidally spread core or the metastable prismatic core, the core transforms to a compact one, due to the strong repulsive effect of the oxygen. (This site is the one between the partials.)
  2. When the oxygen is away from the dislocation centre of the prismatically spread configuration, the core is destabilised and it falls into the ground-state prismatically spread configuration.
  3. The narrowing of spreading (changing to compact core from oxygen near the partials) can be evidenced by Yu, where HAADF-STEM observations found that the dislocation core of titanium was smaller with 0.1wt% oxygen, where oxygen was found in the core vicinity.
  4. Yu *et al* used a cell height of only one burger's vector, so their interaction energies differ from those found by Chaari (3b cell height). The interaction energies are much higher in this work.
  5. In the sites created by the stacking fault ribbon on dissociation, the core configuration is stable.
  6. The third case, where the stacking fault ribbon on the pyramidal plane creates a new site by the pyramidal fault, which correspond to octahedral sites in the twinned hcp crystal. For the pyramidal/mixed prismatic-pyramidal core configurations, where this site is created, one finds that the core remains/becomes close to the mixed prismatic-pyramidally spread core.

## Conclusions

1. Lowest energy core configuration in Ti-O alloys is the pyramidally spread core.
2. Predict that oxygen does not segregate to dislocations in these alloys.
3. When a glissile prismatic core encounters an oxygen atom, the core transforms to one that is pyramidally spread, to avoid the obstacle.

4. This is evidenced by shorter glide distances on the prismatic plane between pinning points in experiments.
5. Due to this cross-slip, jogs are formed, which agrees with *post-mortem* analysis showing that most screw dislocations have jogs in the presence of oxygen. This explains high lattice friction.
6. At higher temperatures, the bypass mechanism will be in competition with oxygen migrating out of the repulsive region, allowing the dislocation to remain in its glide plane.
7. A reconstruction of the pyramidal core induced by interaction with oxygen allows us to understand why cross-slip in pyramidal planes becomes more active with the addition of oxygen. And it can glide in the pyramidal plane by nucleation of kink-pairs.

## 10 What did each method find

## 11

Dislocation-carbon interactions in Fe-C

## Abstract

Martensitic bearing steels have been shown to undergo subsurface microstructural decay, forming Dark Etching Regions (DERs), promoting failure through rolling contact fatigue (RCF). Dislocation-assisted carbon migration is thought to be the underlying mechanism, yet empirical studies have been inconclusive as to how dislocations move carbon and where excess carbon from the martensitic matrix migrates to upon transformation to ferrite—a phase of significantly lower carbon solubility. In this report, we detail the first stages of a multi-scale modelling approach to elucidate carbon transport by dislocations. Tight-binding simulations of carbon interactions with the  $1/2\langle 111 \rangle$  screw dislocation found solute distribution to vary significantly within  $\sim 2b$  of the easy and hard cores; the highest binding energy being found in the centre of the hard screw core—which is the ground state carbon-dislocation configuration—in agreement with Density Functional Theory (DFT). Determination of equilibrium carbon concentration along dislocation lines, at various dislocation densities and nominal carbon concentrations, found most sites around the hard core were saturated, with all easy cores reconstructing to hard due to saturation of adjacent octahedral sites. In the typical temperature range of bearing operation, we expect all dislocations to be of hard core type, pinned by carbon in a prismatic site within the dislocation core. We anticipate large drag forces acting on dislocations in the initial stages of glide, due to carbon-dislocation binding. Line-tension modelling of kink-pair formation shows a small, but consistent, reduction in the kink-pair formation enthalpy with carbon ahead of the dislocation, for all stresses, resulting in a modest increase in average dislocation velocity. In conditions allowing for carbon to equilibrate between trap sites, the average kink-pair formation enthalpy is reduced, increasing dislocation velocity, however a self-consistent method is necessary for accurate results, which is left for future work. For a solute-drag mechanism of dislocation-assisted carbon migration, the reduction in migration energy between carbon sites in the vicinity of a screw dislocation is crucial for its potential validity, such that carbon can keep up with dislocations upon movement. Measurement of these migration barriers using a quantum-mechanical method will provide us with more accurate predicted stress and temperature regimes in which solute drag by screw dislocations is a valid mechanism. These results provide data for the last stage in this multi-scale approach: self-consistent kinetic Monte Carlo (SCKMC) simulations incorporating solute diffusion, to ascertain how carbon moves with dislocations in different stress, temperature and concentration regimes.

## 12 Introduction

Martensitic steels are frequently used in bearings due to their resilience to service conditions, being subject to high rotational speeds and contact pressures. However, under cyclic loading exceeding a given contact stress, the microstructure of the steel can decay due to the accumulation of plasticity. This signals the onset of rolling contact fatigue (RCF), which increases the risk of failure from subsurface crack initiation. The microstructural decay corresponds to the observation of Dark Etching Regions (DERs) as seen in optical microscopy, where the darkness of these regions is due to the higher reactivity of DER phases to the etchant; exacerbated by the roughness of the DER region [?]. See figure 2.

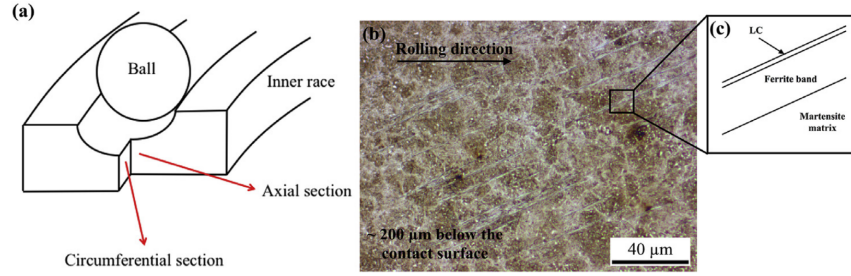


Fig. 2: Diagram of DER location within a bearing and its characteristics, taken from [6]. (a) Axial and circumferential sections of a bearing inner ring. (b) Circumferential section of a bearing inner ring under optical microscope, where ferrite bands (white etching bands) are formed in the subsurface. (c) Diagram showing the structure of a WEB consisting of a ferrite band and a LC adjacent to it. One can see the DER region is composed of regions of ferrite interspersed in the parent martensite with lenticular carbides bordering the ferrite bands.

Decay of the martensitic microstructure is complex, with observation of many different phenomena. Martensite transforms to ferrite microbands as a result of strain localization [6, 7, 8, 9, 10, ?, 11, 12, ?]. Residual carbides, untouched at the start of DER formation, gradually dissolve within ferrite and martensite [9, 10, ?]. Further RCF progression leads to the formation of low and high angle ferrite features, White Etching Bands (WEBs), composed of nanocrystalline [?, ?, ?] and elongated ferrite [?]. Lenticular carbides precipitate at the boundaries of these ferrite bands [10, ?]. Thickening of these carbides occurs during DER development and is correlated with WEB growth [6, 13, 14, 15]. Reductions in dislocation density in nanocrystalline

(heavily deformed) ferrite have been observed in the later stages of DER formation [?, 16].

Carbon migration is thought to be the mechanism by which this degradation occurs, but it is not definitively known how or where carbon migrates with the onset of DER formation. The key questions are: where does excess carbon from the martensitic matrix find itself when the structure decays to low solubility (0.02 wt%) ferrite? and how is the carbon transported, given its low diffusivity in martensite/DER phases [17]?

Fu *et al.* propose that carbon atoms inside the martensite would segregate to pre-existing/residual carbides, increasing their size [13]. This theory was successfully applied to the growth of lenticular carbides [6], however, problems arise with the application to temper carbide growth: if carbides were to form in martensite, they should follow the Bagaryatskii/Isaichev orientation relationship, but observations suggest a lack of any orientation relationship [18]. Temper carbides residing within DERs have irregular shapes/diffuse boundaries, which are seemingly due to the incomplete dissolution of temper carbides, which is at odds with the theory of Fu *et al.*.

A plausible mechanism for carbon migration is that it is driven by dislocation glide, which is as follows [6, 10, 11, 13, 14, 15]. Due to the high dislocation density exhibited in martensite, carbon segregates to dislocations in Cottrell atmospheres, causing pinning. Strain generated by cyclic stresses allow dislocations to escape their carbon rich environment. The free dislocations re-attract carbon, allowing the Cottrell atmospheres to reform, subsequently re-pinning the dislocations, creating a net carbon flux. This mechanism allows for the movement of carbon during the martensite-ferrite transition, while also explaining how excess carbon can move from the ferrite phases to lenticular carbides at the boundaries, describing the process behind both WEB growth and carbide thickening. Moreover, it explains the dissolution of residual carbides, both in ferrite WEBs and martensite, due to dislocation rearrangement and pile ups at the carbide interface drawing carbon atoms out, due to a more favourable binding to dislocations. However, as to how this process occurs on the atomistic scale, or if it is indeed feasible, is unknown.

Experimentally probing dislocation-assisted carbon migration has proven difficult and inconclusive. Work needs to be done to understand dislocation-carbon interactions; more specifically: how dislocations move carbon within the temperature and stress regimes experienced during operation; where carbon is transported to and what the resultant dislocation networks are.

To shed light on this mechanism, a multi-scale modelling approach can be used. Atomistics can provide information of the 2d Peierls energy landscape



which dislocations are subject to in iron; and how this landscape is modified by the binding of carbon to dislocations. This data can be used in a line tension model of a dislocation to determine the kink-pair formation energies of dislocations as a function of carbon content and stress. Finally, one can use a kinetic Monte Carlo (kMC) model of dislocation glide by thermally activated kink-pair nucleation, in an environment of carbon. From this last stage of coarse-graining, one can determine in which regimes of temperature, stress and carbon concentration, dislocation-assisted carbon migration becomes a feasible mechanism behind DER formation, with predictions of dislocation velocity, dislocation configurations and where carbon moves with dislocation glide.

In this report, we will focus on the atomistic portion of this project, directed at understanding dislocation-carbon interactions at the atomistic scale in ferrite (bcc iron). With further knowledge of the fundamental mechanism behind DER formation, we can hope to suppress dislocation motion in the martensitic matrix, mitigating failure by RCF.

## 13 Computational Method

We use the tight-binding model of Paxton and Elsässer [5], which has been shown to describe the binding energies of carbon complexes in bcc iron, in good agreement with DFT calculations. This model reproduces the two screw dislocation core structures—the easy and hard  $1/2\langle 111 \rangle$  cores—exhibited in bcc iron. Study of both is crucial to understanding solute-dislocation interactions. The easy core is the ground state in pure iron, but solutes, such as hydrogen and carbon, have been shown to reconstruct this core into the hard core configuration [19, 20]. Computationally cheaper models, which do not incorporate quantum mechanics, such as the EAM, cannot reproduce these behaviours.

### 13.1 Peierls Potential

To determine the Peierls potential of the  $1/2\langle 111 \rangle$  screw dislocation, we followed the procedure detailed in Itakura [21]. Quadrupolar arrays of dislocations were constructed by placing dislocations of antiparallel  $1/2\langle 111 \rangle$  Burgers vectors in an "S" arrangement [22], with initial displacements determined by anisotropic elasticity solutions. See figure 3, left. A quadrupolar arrangement minimises the stress each dislocation experiences in the simulation. These displacements were modified to be periodic, thereby removing artificial stacking faults which would appear between periodic images after

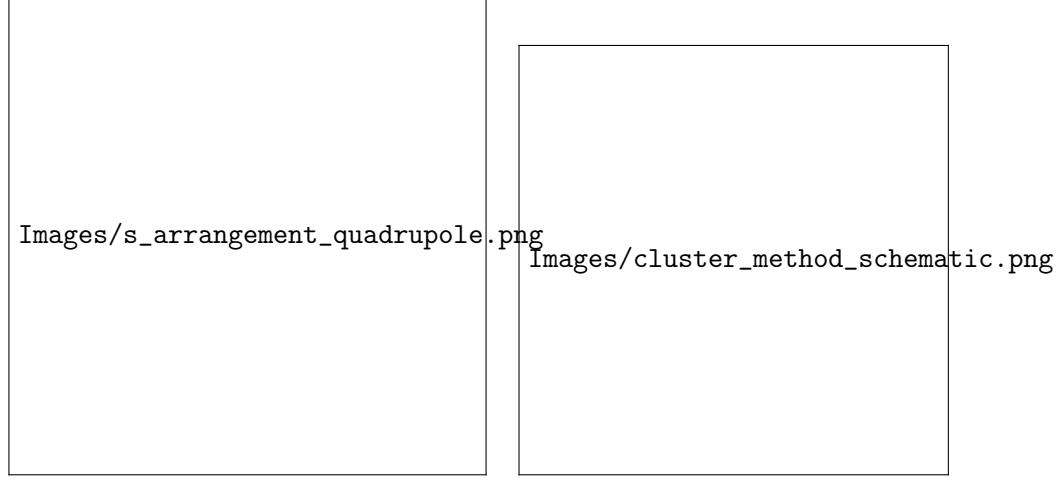


Fig. 3: Schematics of dislocation simulation methods. Left: quadrupolar arrangement of dislocations in a simulation cell (grey square). This arrangement minimises the stress experienced by each dislocation in a periodic simulation. Cell vectors  $\vec{U}_1$  and  $\vec{U}_2$  are shown;  $\vec{A}$  defines the cut plane between the dipoles. The dislocation positions, and their corresponding burger's vector direction, are denoted by the symbols  $\otimes$  and  $\odot$ , which are antiparallel to each other. Tilt components added to cell vectors to accomodate for the plastic strain are not shown. Right: cluster method, where atoms are displaced according the displacement field from the screw dislocation at the centre of the cluster, denoted by "\$". Atoms in the annulus  $R_2 - R_1$  are fixed in position to the anisotropic elasticity solutions. Within  $R_1$ , all atoms can relax. Periodicity is only imposed in the  $Z$  direction.

introduction of the dislocation dipole. This was achieved by the subtraction of a linear error term from the superposition of displacement fields arising from the dislocations in the simulation cell and its periodic images [23]. To accommodate for the internal stress upon introduction of a dislocation dipole into the simulation cell, an elastic strain was applied to the cell, resulting in an additional tilt component to cell vectors [22, 23, 24]. Simulation cells were constructed with different initial core positions, which were sampled from the triangular region "EHS" (easy, hard and split) core positions, as detailed in figure 4. To fix the dislocation positions during relaxation, the three atoms surrounding the easy core, for each dislocation, were fixed in  $Z$  coordinate during relaxation, where  $Z$  is a  $\langle 111 \rangle$  direction, along the dislocation line. The k-point sampling mesh for each of these cells was  $5 \times 5 \times 30$ .

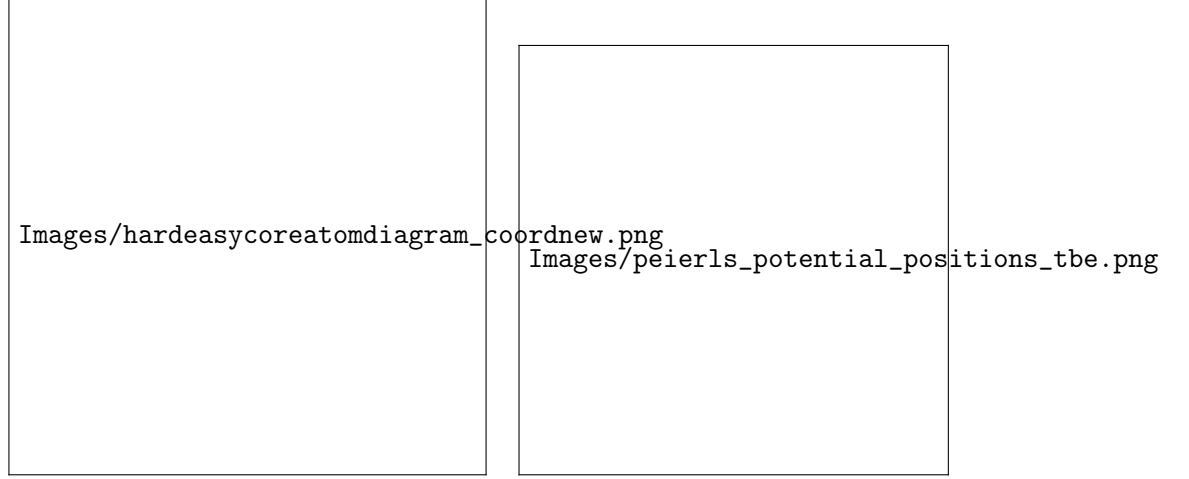


Fig. 4: Diagrams of dislocation core positions. "E", "H" and "S" correspond to the easy, hard and split core positions respectively. Left: core positions as seen along the  $Z = \langle 111 \rangle$  direction, along the dislocation line. Atomic positions are shown as grey circles. Right: positions sampled within the triangle EHS used to determine the Peierls potential.

The interaction energy between the dislocation dipole and periodic images was defined differently to Itakura [21]. We followed the prescription of Bulatov and Cai [23] to find a regularised interaction energy, which is independent of truncation limit, in contrast to the formulas quoted in Itakura's papers. Details can be found in section 20.

The Peierls potential  $\Delta E_P^i$ , for an isolated dislocation at the  $i^{\text{th}}$  core position, can be calculated from

$$\Delta E_P^i = \Delta E_{\text{tbe}}^i - \Delta E_{\text{INT}}^i, \quad (4)$$

where  $\Delta$  refers to quantities, per dislocation, relative to the relaxed easy core configuration (labelled as E/1, as in figure 4). *e.g.*  $\Delta E_{\text{tbe}}^i = \frac{1}{2}(E_{\text{tbe}}^i - E_{\text{tbe}}^{\text{E}})$  is the difference in energy, per dislocation, between a relaxed cell which has the two dislocation cores placed at position  $i$ ,  $E_{\text{tbe}}^i$ , and a relaxed cell which has the two cores placed in easy core positions  $E_{\text{tbe}}^{\text{E}}$ , divided by the number of dislocations in each of the simulation cells. Dislocation-dislocation interaction energies are included in this term, due to dislocations in the simulation cell—and periodic images—interacting with each other, as can be readily seen in figure 3. To model the energy landscape of an isolated dislocation, these interaction energies must be subtracted, which is achieved

by the correction term  $\Delta E_{\text{INT}}^i = \frac{1}{2}(E_{\text{INT}}^i - E_{\text{INT}}^{\text{E}})$ .

### 13.2 Preliminary calculations

To determine the binding energy of carbon to dislocations, we used the cluster method, as shown in figure 3, right. Simulation cells consisted of a cylindrical cluster of atoms, with a single dislocation introduced into the centre using displacements from anisotropic elasticity solutions. Each of the clusters were centred on the easy or hard core positions. The cluster of atoms was split into two regions: a central region of dynamic atoms with radius  $R_1$ , and an annulus of atoms, between  $R_1$  and  $R_2$ , which were fixed in position to the displacements from anisotropic elasticity.

To confirm the anisotropic elasticity solutions were correct, we compared the displacements against the analytic solutions to the straight screw dislocation, as given in Hirth and Lothe [?]. Furthermore, energy scaling relations were verified. We inserted dislocations into cells of varying radii:  $R_1 = x\sqrt{2}a_{\text{bcc}}$ , and  $R_2 = (x+1)\sqrt{2}a_{\text{bcc}}$ , where  $x \in \{2 \dots 5\}$ . The excess energy was defined as the energy difference of a cell with a dislocation inserted,  $E_{\text{d}}$ , with respect to a perfect cell reference energy of the same geometry,

$$E_{\text{excess}} = E_{\text{core}} + E_{\text{elastic}} = E_{\text{d}} - E_{\text{perfect}}, \quad (5)$$

where  $E_{\text{elastic}} = (\mu b^2/4\pi) \ln(R/r_c)$ , with  $R = R_2$  and  $r_c = b$ .

Initially, large cells of  $R_1 = 6\sqrt{2}a_{\text{bcc}}$ , and  $R_2 = 7\sqrt{2}a_{\text{bcc}}$  with depth of single burger's vector, were relaxed for both the easy and hard cores, which consisted of 522 and 540 atoms respectively. The three atoms surrounding the core were constrained to only relax in  $X-Y$  plane, to fix the dislocation upon relaxation. The k-point sampling mesh for each of these cells was 1x1x24.

From the relaxed cells, a smaller region of 174 atoms, with  $R_1 = 3\sqrt{2}a_{\text{bcc}}$ , and  $R_2 = 4\sqrt{2}a_{\text{bcc}}$ , was cut from the dynamic regions. This smaller cell was extended to a thickness of  $3b$  in the  $Z$  direction. Carbon interstitials were inserted into octahedral sites near the dislocation core, in the middle layer. Exploiting reflection and rotational symmetry, only 10 interstitial sites needed to be used to obtain the binding energies of carbon  $\sim 2$  b from the core, denoted by  $iHj$  and  $iEj$ , where  $j \in \{1 \dots 10\}$ . The final binding sites are denoted by  $Hk$  and  $Ej$ , where  $k \in \{1 \dots 7\}$ . The three atoms surrounding the core in the first and third layers were again constrained to relax only in the  $X$  and  $Y$  directions. No such constraints were imposed on the middle layer.

Interestingly, if one to pre-emptively include the distortion carbon into the cell, by superposing the displacement field generated from carbon in an otherwise perfect cell of 3b length—one does not find the true ground state structures, as predicted by dipole calculations which allow all degrees of freedom to be relaxed.

### 13.3 Fe-C binding energies

We calculated the carbon-dislocation binding energies as in Itakura [20].

The binding energy is given by

$$E_b = -(E_{d+C} + E_{\text{perfect}} - E_d - E_{C \text{ ref.}}), \quad (6)$$

where  $E_{d+C}$  is the total energy of a relaxed cluster with a carbon interstitial and a dislocation,  $E_d$  is the total energy of a relaxed cluster with a dislocation and  $E_{C \text{ ref.}}$  is the total energy of a relaxed perfect cluster with a single carbon in an octahedral site. A positive binding energy indicates favourable binding.

The zero-point energy (ZPE) is calculated as in Itakura. Details can be found in 21. The ZPE corrected binding energy is given by

$$E_b^Z = E_b + \Delta E_z,$$

where  $\Delta E_z = E_z - E_z^{\text{C ref.}}$  and  $E_z^{\text{C ref.}} = 202.5\text{meV}$  is the zero-point energy of carbon situated in an octahedral site in a perfect cluster of the same size.

Calculations were also

### 13.4 Carbon concentration on dislocation line

Using the Fe-C binding energies, one can predict the equilibrium carbon concentration of a carbon binding site  $c_d$ , using a thermodynamical mean-field model [?, 19, ?], under the assumption that carbon atoms around the core are sufficiently spaced such that intersite interaction energies are negligible.

The concentration is given by,

$$\frac{c_d^i}{1 - c_d^i} = \frac{c_{\text{bulk}}}{1 - c_{\text{bulk}}} \exp\left(\frac{-E_{\text{seg}}^i(c_d)}{k_B T}\right), \quad (7)$$

where  $i$  denotes the  $i^{\text{th}}$  carbon binding site.  $E_{\text{seg}}^i$  is the mean segregation energy defined as

$$E_{\text{seg}}^i(c_d) = -E_b^i + 2c_d V_{CC},$$

where  $E_b^i$ , is the corresponding dislocation-solute binding energy (in the convention of attraction denoting a positive binding energy).  $c_d^i$  is the average concentration of the  $i^{\text{th}}$  carbon site bound to dislocations.  $c_{\text{bulk}}$  is the carbon concentration in the bulk, with  $c_{\text{nom}}$  the nominal carbon concentration per Fe atom.  $V_{\text{CC}} = 0.30\text{eV}$  is the carbon-carbon first-neighbour repulsion term, which is calculated as in Ventelon [19]. This repulsion term was calculated from carbon in the H1 prismatic site. It was assumed that this repulsion term is the same for carbon in the E2 site.

In a given volume  $V$ , the number of carbon sites along the dislocation cores is given by  $N_d = \rho V/b$ , with  $\rho$  the dislocation density, and the number of octahedral sites is  $N_{\text{oct}} = 6V/a_{\text{bcc}}$ . This imposes constraints on the carbon concentrations:  $N_{\text{oct}}c_{\text{bulk}} + N_dc_d = N_{\text{oct}}c_{\text{nom}}/3$ , where the factor of 3 is because there are three octahedral sites per Fe atom in the bcc lattice. Using this relation, equation (7) can be solved self-consistently to give the carbon concentration around the core, as a function of nominal carbon concentration and temperature. The nominal carbon concentration was taken to be the maximum solubility of ferrite in the DER region,  $0.02 \text{ wt}\% \approx 1000 \text{ appm}$  [17]. Calculations of 10 and 500 appm were also performed. The dislocation density was varied between  $1 \times 10^{12}$ ,  $1 \times 10^{14}$  and  $5 \times 10^{15}$ , to see the effects of low densities up to the upper bound of dislocation densities  $\sim 5 \times 10^{15}$  found in Fe-0.61wt%C martensite [25].

Further discussion on carbon concentration formulations is given in section 13.5.2.

### 13.5 Line Tension Model

The kink-pair formation enthalpy is defined as the minimum energy necessary to create a kink-pair from a dislocation in a Peierls valley. One can find this by sampling the energy landscape seen by a dislocation line which moves one peierls valley to the next, from which the minimum enthalpy path can be sought. The difference between the maximum enthalpy image, corresponding to a dislocation configuration in a transition state, and enthalpy of the initial state, is the kink-pair formation enthalpy. One can efficiently determine the minimum enthalpy path using the String/Nudged Elastic Band (NEB) algorithms. In these methods, a set of images, which interpolate between the initial and final states, are relaxed along the energy landscape.

From atomistic calculations of the Peierls potential and carbon-dislocation binding energies, one can construct a line tension model of a dislocation from which we can obtain the kink-pair formation energies as a function of stress and carbon content [?, 21, 20]. This model views the dislocation as

an elastic chain which moves in the Peierls potential  $\Delta E_P$ . Models of this type—consisting of a one-dimensional chain of particles with spring force interactions between nearest-neighbours, in a substrate potential—are also called Frenkel-Kontorova models, and have been crucial in some of the first investigations into kink-pair formation, among other non-linear processes [?, ?, ?, 26].

The dislocation is modelled as a discretised line, with layer labels  $j$ . The energy of the dislocation line is given by:

$$H_{LT}(\sigma) = \frac{K}{2} \sum_j (\vec{P}_j - \vec{P}_{j+1})^2 + \sum_j \Delta E_P(\vec{P}_j) + (\sigma \cdot \vec{b}) \times \vec{l} \cdot \vec{P}_j - \sum_{j,k} E_C(|\vec{P}_j - \vec{P}_k^C|),$$

where  $K$  is a constant calculated from atomistics,  $\Delta E_P$  is the Peierls potential,  $\sigma$  is the stress applied and  $\vec{b}$  is the burger's vector, with the dislocation line sense given by  $\vec{l}$ .  $\vec{P}_j$  corresponds to the dislocation core position in a given layer.  $E_C(|\vec{P}_j - \vec{P}_k^C|)$  is the binding energy of a particular carbon  $k$ , at position  $\vec{P}_k^C$ , to a dislocation core positioned at  $\vec{P}_j$ . The kink-pair formation enthalpy can then be found using the string method to relax images which interpolate between the initial and final states (straight dislocations in adjacent peierls valleys), to find the height of the transition-state barrier. A `julia` implementation of the string algorithm, accelerated by use of an ODE solver, was used to relax the images [27]. The implementation was validated on the dataset of Itakura [21].

### 13.5.1 Line-tension model in carbon environment

Dislocations form Cottrell atmospheres of carbon, which influence their motion. Analysis of the dynamics of a dislocation moving from one Peierls valley to the next, in an environment of carbon in equilibrium with the bulk, can provide estimates of: the mean energy barrier experienced by a straight dislocation segment upon glide, and the mean kink-pair formation enthalpy, both as functions of nominal carbon concentration. Results of the latter can be used as inputs to a self-consistent kinetic Monte-Carlo (SCKMC) model of dislocation glide, which has been shown to predict dislocation structures in hydrogen-charged iron [?]. The kink-pair formation enthalpy calculations in this paper study were performed in the limit of slow dislocation glide, allowing carbon to equilibrate between sites, however more accurate results may be possible by accounting for dislocation velocity in a self-consistent manner.

The binding sites of carbon around the easy and hard core dislocation positions were found from atomistic simulations, detailed in section 14.3. Movement of a dislocation between peierls valleys generates intermediate core positions which lie between the easy and hard cores. Carbon trap sites are not well-defined for these intermediate dislocation positions. To circumvent this, trap site positions were smoothly mapped between the easy and hard core positions by use of the dislocation core coordinate  $P_x$ . Further information on the mapping of sites can be found in appendix .

The carbon concentration on the dislocation line was calculated by the self-consistent thermodynamical mean-field model, detailed in 13.4. The concentration was fixed to the value obtained using the H1 binding energy,  $c_{\text{total}} = c_d^{\text{H1}}$ , imposing the assumption that the dislocation neither rejects or absorbs carbon, despite changes in the carbon environment upon core movement. Thus carbon concentration on the dislocation line remained in equilibrium with the bulk during the simulations.

The equilibrium concentration of carbon in a trap site  $i$ ,  $c_i^e$  was initially determined by use of Maxwell-Boltzmann statistics [?], as done by Cottrell and Bilby [?], and Gong [?],

$$c_i^e(x) = c_d^{\text{H1}} \frac{e^{-E_i(x)/k_b T}}{\sum_j e^{-E_j(x)/k_b T}}.$$

These concentrations modify the interaction energy of a given site multiplicatively, such that the total interaction energy of a dislocation in an environment of solutes is given by

$$E_{\text{INT}}^e = \sum_j c_j^e E_j(x).$$

Kink-pair formation enthalpies were obtained using the string method, as detailed in section 13.5.

### 13.5.2 Extension to more Fermi-Dirac statistics

Cottrell and Bilby’s assumption of Maxwell-Boltzmann statistics, as seen in equation (13.5.1), is valid for small dislocation-solute binding energies, which are generally found for solutes far from the dislocation [?]. However, close to the dislocation core, we expect a strong binding of carbon to dislocations, as such, Maxwell-Boltzmann statistics fails to be a good description of carbon occupancies: one finds unphysically large occupancies, due to carbon being able to occupy the same site [28].



For a more realistic description of carbon occupancies, one must account for the limited number of carbon sites close to the dislocation core, which are either occupied or not. This problem, of distributing indistinguishable particles (neglecting inter-/intra-site interactions) between sites which can only be singly-occupied, is reminiscent of Fermi-Dirac statistics, which was applied by Nematollahi [28] to treat carbon occupancies around an edge core up to a cut off of 0.04—a result obtained by the EAM calculations of Veiga [29]. This distribution was assumed to be true, however, it neglected the effect of assumptions which were not explicitly taken into account. Louat [?] provided a more rigorous derivation for the concentration of solutes close to the dislocation core, which has been used by many in recent years [19, ?, ?, ?, ?]. In this formulation, it is assumed that the area around the dislocation is divided into a number of sub-regions (an effective lattice) where only one solute atom can occupy each position, and there are no inter-line or inter-site interactions. One only accounts for the configurational entropy of the effective lattice; electronic, vibrational and magnetic entropic contributions are not taken into account [19]. This treatment of configurational entropy becomes inaccurate for low binding energies, as noted the case of hydrogen/hydrogen-vacancy complexes in Fe [?]: with low enough binding energies, the species is able to move in a smooth and continuous potential, resulting in a larger configurational phase space available than just the sampled binding sites taken into. We expect due to the large binding energy of carbon to dislocations, relative to hydrogen, for a range of distances, the configurational entropy would not be significantly enhanced compared to the lattice model.

## 14 Results

### 14.1 Peierls Potential

Comparison of 2d Peierls potentials of the  $1/2\langle 111 \rangle$  screw dislocation between DFT and tight-binding models can be found in figure 5, with data found in table 2. The sampled energies were interpolated using 2d cubic splines. The relative energies between the different core positions was found to be smaller in both tight-binding models compared to DFT. These are artifacts of the models, which have been reproduced in atomistic NEB calculations of the  $1/2\langle 111 \rangle$  screw dislocation Peierls barrier using the canonical  $d$ -band model: the Peierls barrier in this model is approximately half that of DFT [30].

The Peierls potential of the  $d$ -band model was found to be more reminiscent of DFT, compared to the  $s$ - $d$  model; but the deviation is small: the

Images/peierls\_potential\_dft\_labelled\_zeal.png

Images/peierls\_potential\_sdTB\_labelled\_zeal.png

Images/peierls\_potential\_dTB\_labelled\_zeal.png

Fig. 5: Comparison of 2d Peierls potentials of the  $1/2\langle 111 \rangle$  screw dislocation between DFT [21] (top) and tight-binding (*sd* non-orthogonal middle, canonical *d*, bottom).  $x - y$  axes in units of  $d = a\sqrt{2}/3$ . Energy scale is in meV. "E", "H" and "S" correspond to easy, hard and split core positions respectively, with the latter also corresponding to atomic positions. The relative energies between the different core positions is smaller in tight-binding compared to DFT. The split core as seen in tight-binding is reminiscent of FAM potentials, where the split core energy is lower than that of the hard

maximum difference between the  $d/s$ - $d$  models being  $\sim 10$  meV, with the  $d$ -band model being, on average,  $\sim +3$  meV higher.

The split core energy is lower than that of the hard core, which is reminiscent of EAM potentials [21], but not as severe, as seen in figure 6. Some of this discrepancy can be attributed to the erroneous interaction term included by Itakura, as detailed above—interaction energies can become arbitrarily high, if not made independent of truncation limit—but likely there are effects in DFT which are not encapsulated fully within the tight-binding description, such as a lack of core electron repulsion upon deformation of the lattice, which would increase the relative energy difference. Consequences of this discrepancy on future kMC simulations are discussed in section 15.

Table 2: Table of energies used to calculate the Peierls potential. All values in meV.  $\Delta E_{\text{P}}^{\text{DFT}}$  values taken from [21].

Pos	$\Delta E_{\text{INT}}$	$\Delta E_{\text{tbe}}$	$\Delta E_{\text{P}}^{sd}$	$\Delta E_{\text{P}}^d$	$\Delta E_{\text{P}}^{\text{DFT}}$
1	0	0	0	0.0	0
2	-0.7	7.3	7.9	6.3	3.2
3	-1.4	16.0	17.4	15.1	19.2
4	-2.0	22.2	24.2	20.4	31.1
5	-2.5	24.8	27.4	22.6	39.3
6	-3.3	3.0	6.3	4.6	11.5
7	-6.5	7.1	13.6	12.7	39.9
8	-9.6	13.0	22.6	22.7	75.2
9	-12.5	5.4	17.9	26.8	108.9
10	-4.8	22.1	26.9	23.0	34.8
11	-7.2	18.2	25.4	23.5	37.9
12	-9.8	14.0	23.8	24.4	60.7
13	-3.8	11.5	15.3	13.2	17.6
14	-6.9	15.1	22.0	20.3	29.9
15	-4.3	18.6	22.9	20.0	39.7

The transitional kink shape from the  $s$ - $d$  and  $d$ -band Peierls potentials may differ compared to DFT, with dislocation core positions possibly being situated closer to the split core position, similar to EAM potentials [21, ?]. Following the Peierls potential along the H-S direction, as seen in figure 6, we see that the Itakura potential has a saddle point minimum, which corresponds to the dislocation core positions found upon kink-pair formation [21]. In the  $s$ - $d$  model, the Peierls potential decreases monotonically along the H-S line and there is a subtle maximum found in the  $d$  – band model.

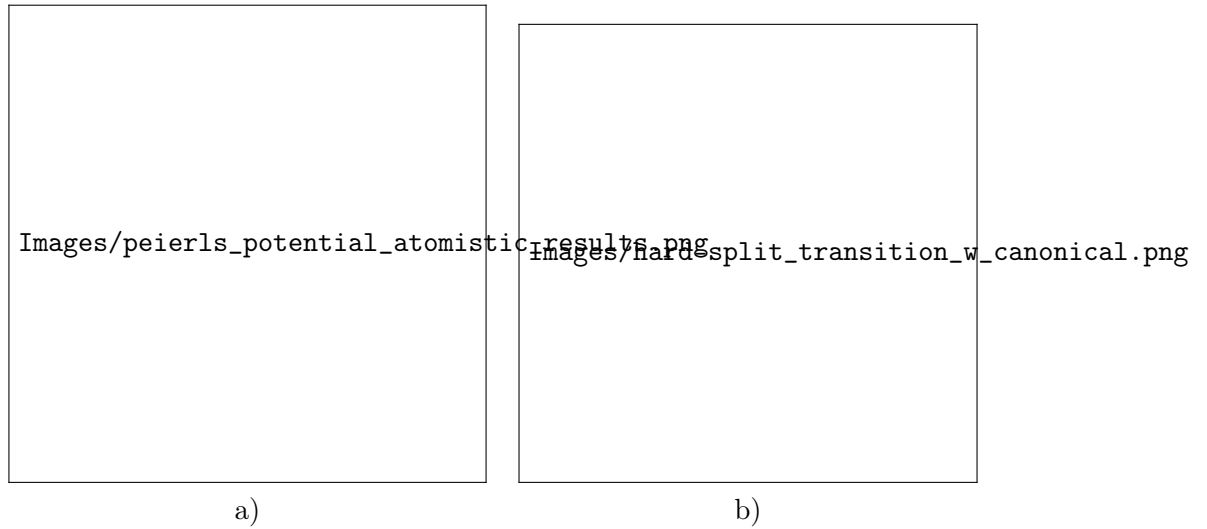


Fig. 6: Left: Peierls barriers from atomistic calculations using canonical- $d$ -band tight-binding, DFT and the Mendelev EAM potential, plots of the corresponding dislocation pathways can be found in figure 14. The EAM potential of Mendelev [?] has an unphysical well in the centre of the potential, while tight-binding and DFT produce single-humped potentials. Right: Peierls potential along the hard-split line. One can see in  $s$ - $d$  tight-binding model pathway is similar in shape to the EAM potential of Mendelev [?]: it decreases consistently from the hard core to the split core. In DFT one finds a saddle point between the hard core and the midpoint.

This data suggests there may be a deviation in the dislocation path found in DFT, in moving from one Peierls valley to the next along the H-S line. Atomistic calculation of the Peierls barrier between two easy core positions in the canonical  $d$ -band model found core positions of the transitional kink state to go through the metastable point, similar to DFT [30], which suggest the deviation may not be severe. Section 14.5 discusses the effect the Peierls potential has on the pathway taken by a dislocation moving from one Peierls valley to the next.

## 14.2 Preliminary calculations

To validate the cluster simulation method, the excess energy, defined as the difference in energy between a cell with a dislocation, and a perfect reference cell, was plotted as a function of  $\ln(R/r_c)$ , where  $R = R_2$  of the cluster and  $r_c = b$ , as seen in figure 7. In isotropic elasticity theory, this should give a linear dependence where the gradient corresponds to  $\mu b^2/4\pi$ , with the  $y$  intercept corresponding to the core energy  $E_{\text{core}}$ . This is well reproduced by our model, except at low  $\ln(R/r_c)$  as expected, where the cell size is not large enough to accommodate for sufficient relaxation of the dislocation core, increasing the core energy, which is not accounted for in elasticity theory.

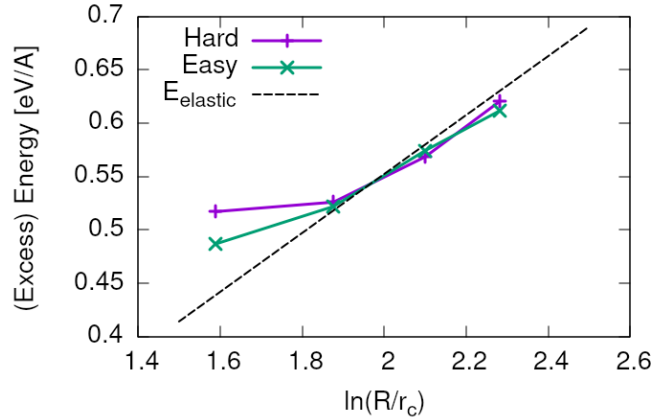


Fig. 7: Excess energy of dislocation clusters with differing radii for both the easy and hard core configurations. The prediction from elasticity theory is given by the black, dashed line. Deviation of both cores occur when cell size is small, creating an increase in the core energy, which elasticity theory cannot account for.

The energy cost to transform from the easy to the hard core can be estimated by the difference in excess energies between the cores in the limit of  $\ln(\frac{R}{R_0}) \rightarrow 0$ . At the smallest measured value, one finds that the core energy difference  $\Delta E_{\text{core}}^{\text{Easy-Hard}} = 76 \text{ meV/b}$ , which is in good agreement with the DFT value of  $82 \text{ meV/b}$  [21].

For a line tension model of a dislocation, it is necessary to ascertain the energy, denoted  $E_L = E_{\text{el}} + E_{\text{core}}$  as in Provile [26]. This can be obtained by subtracting the total energies of relaxed dislocation configurations to obtain the core energy.

### 14.3 Fe-C binding energies

As found in DFT simulations by Ventelon [19], when a carbon was placed in the vicinity of a relaxed easy dislocation core—in either of the two nearest, distinguishable, octahedral sites—a spontaneous reconstruction of the dislocation core occurred: from easy to hard. Upon reconstruction, the dislocation core moved to a neighbouring triangle, when looking along the  $\langle 111 \rangle$  direction, where the carbon found itself situated in the centre. This will be called a prismatic site, as in Ventelon’s paper. This confirms that both hard and easy dislocation cores must be studied to fully understand screw dislocation behaviour in bcc iron.

The binding energies of carbon to both the hard and easy cores can be seen in table 4, with the resulting distribution of carbon in figures 8 and 9. The distribution of carbon strongly depends on the type of core it finds itself situated near. The easy core only significantly modifies the position of the iE1 site, to the E1 site, situated in the centre of an adjacent triangle. All other sites are unaffected, so there is a one-to-one correspondence between all iEj and Ej sites, where  $j \in \{2 \dots 10\}$ . There are carbon basins available close to the triangular region containing the core, but not inside.

Carbon favours a prismatic site within the hard core (H1), which has the highest binding energy,  $1.29 \text{ eV}$ , of all sites considered. There are no binding sites apparent in a triangular annulus (of width  $a_{\text{bcc}}\sqrt{2}/2$ ) surrounding the hard core triangle due to the destruction/volume reduction of octahedral sites near the hard core. The initial octahedral sites, iH1 and iH2 decay to the H1 site. Similarly, iH3 and iH4 decay to the H2 site, with iH9 and iH10 decaying to a H7 site. Relations between each of the sites is given in table 3.

Note that interactions between carbon atoms around the core are not taken into account here: figures 8 and 9 are purely diagrammatic and not what one expects the true distribution of carbon around a screw dislocation

Table 3: Decay relations between the initial and final sites upon relaxation of carbon interstitials around the hard core.

Initial	Final
iH1, iH2	H1
iH3, iH4	H2
iH5	H3
iH6	H4
iH7	H5
iH8	H6
iH9, iH10	H7

would be. Carbon is strongly repulsive at first nearest-neighbour distances, which would modify each of these distributions.

These binding energies agree well with experiment and atomistic/elastic calculations. EAM simulations by Clouet [31, 32] found a maximum binding energy of 0.41 eV by calculating the elastic dipole tensor within Eshelby theory. Hanlunmyuang et al. [33], similarly conducted DFT and EAM calculations for the interaction energy 12Å from the core, and their calculations agreed with the continuum limit of Eshelby theory with a binding energy of 0.2 eV. In DFT calculations by Ventelon [19], the interaction energy of a carbon in a hard core prism configuration was found to be 0.79 eV for a thickness in the  $Z$  direction of  $3b$  (0.73eV for  $6b$ )—in the convention that a positive binding energy indicates attraction. This is significantly lower than the 1.29eV interaction energy of tight-binding. This discrepancy can be partially explained by the fact that the cells have not been allowed to relax with all degrees of freedom, as in the Ventelon results: the three atoms around the screw core are fixed in  $Z$  so the dislocation core position does not change upon relaxation.

Repeating the calculation for the binding of a H1 carbon to a screw dislocation using a quadrupolar array, allowing for all atoms to relax, gives a binding energy of 0.88 eV. This agrees very well with the DFT results of Ventelon [19].

A source of error for this discrepancy is likely from the fitting of the tight-binding model itself. The Peierls barrier of this  $s$ - $d$  model of iron, necessary for Fe-C interactions, has been shown to be half that found in DFT [30], but the solution energies for Fe-C defect complexes are well described. This implies there is insufficient repulsion between Fe-Fe species upon deformation, leading to a larger resultant Fe-C binding energy from tight-binding.



Fig. 8: Initial (top) and final (bottom) positions and binding energies (eV) of carbon around the easy core. Binding energies are not shown for the initial positions. Top: initial positions before relaxation. Bottom: final positions and binding energies after relaxation. The core was constrained by fixing the top and bottom three atoms surrounding each of the cores. As shown by Ventelon [19], the first and second closest octahedral sites to the hard core decay to a prismatic position inside the hard core





Fig. 9: Initial (top) and final (bottom) positions and binding energies (eV) of carbon around the hard core. The core was constrained by fixing the three atoms surrounding each of the cores in the top and bottom layers. As shown by Ventelon [19], the first and second closest octahedral sites to the hard core decay to a prismatic position inside the hard core.

Site Type	distance from core [b]	$E^z$ [eV]	$\Delta E^z$ [eV]	$E_b$ [eV]	$E_b^z$ [eV]
E1	0.57	0.185	-0.018	0.793	0.775
E2	0.70	0.202	-0.001	0.793	0.793
E3	0.99	0.205	0.002	0.137	0.139
E4	1.21	0.208	0.005	0.229	0.234
E5	1.36	0.210	0.008	0.784	0.791
E6	1.66	0.209	0.007	0.597	0.603
E7	1.89	0.206	0.003	0.385	0.388
E8	1.77	0.203	0.000	0.177	0.178
E9	1.52	0.201	0.000	0.683	0.683
E10	1.95	0.202	0.000	0.067	0.067
H1	0.00	0.196	-0.006	1.298	1.291 [ 0.881 <sup>a</sup> , 0.790 <sup>b</sup> ]
H2	1.19	0.210	0.007	0.691	0.698
H3	2.12	0.209	0.007	0.461	0.467
H4	1.91	0.207	0.005	0.311	0.316
H5	1.80	0.208	0.006	0.403	0.409
H6	1.40	0.207	0.005	-0.119	-0.114
H7	1.35	0.206	0.006	0.825	0.819

Table 4: Table of energies leading to the zero-point energy corrected binding energy using the cluster method for simulation of dislocation-carbon interactions. <sup>a</sup> Tight-binding quadrupolar array results, starting from a fully relaxed easy core quadrupole extended to a depth of 3b with carbon introduced into the iH1 site in the middle layer, by both dislocations. <sup>b</sup> DFT results of Ventelon, using the same quadrupolar configuration as in <sup>a</sup>. In both quadrupolar simulations, carbon ended up in the H1 site.

## 14.4 Carbon concentration along on line

The variation of carbon concentration along the dislocation line for the highest binding energy sites of the easy and hard cores can be seen in figure 10. We see at low temperatures, all dislocations are decorated with carbon. As temperature increases, the amount of carbon decorating the dislocations starts to decrease. Due to the lower binding energy of carbon to the easy core, desaturation occurred at a lower temperature compared to the hard core. Dislocation densities near the upper bound of what has been observed in martensite,  $\rho \approx 10^{15}$ , reduce the temperature at which carbon concentration starts to decrease on the dislocation core. Lower nominal carbon concentrations cause carbon concentrations around the dislocation to decrease at a lower temperature.

In the high-purity iron case,  $C_{\text{nom}} = 10$  appm, we find at dislocation densities above  $\rho \approx 10^{15}$ , that there is a reduction in the maximum concentration permitted in the material, with increasing dislocation density. This is due to the fact that there is not enough carbon for all of the dislocations, as such the concentration on the dislocation line drops.

In the operating temperature range of  $40-90$  deg C =  $310-360$  deg K, we expect most hard core sites are saturated. Given the high concentrations of the E1/E2 sites around the easy core in this range, we expect all dislocations will be of the hard core type, due to reconstruction of the easy core by the adjacent carbon.

## 14.5 Line Tension Model

\* Insert here what the line tension model neglects in terms of energetics \*

### 14.5.1 Prerequisites

The  $K$  coefficient for the line tension model was calculated from atomistic simulations, using the method of Itakura [21], by calculation of a Hessian from the displacement of atoms surrounding the dislocation core. Tight-binding gave  $K = 0.734 \text{ eV}\text{\AA}^{-2}$ , which agrees well with DFT, where  $K = 0.816 \text{ eV}\text{\AA}^{-2}$ .

||

Dislocation-carbon binding energies were found to decay with distance, as seen in figures 11 and 12. A Lorentzian was fit to specific binding energies such that a continuous function could be used to describe binding within the line tension model. This is a purely empirical model. The choice of sites used for the fitting is discussed in section 15.

Images/mcclean\_isotherm\_all\_e2\_h1.png

Fig. 10: Variation of carbon concentration on the dislocation line  $c_d$  for the highest-energy binding sites for the hard core (H1) and easy core (E2). Solid, dashed, dotted and dash-dotted lines correspond to dislocation densities of  $1 \times 10^{12}$ ,  $1 \times 10^{14}$ ,  $1 \times 10^{15}$  and  $5 \times 10^{15}$  respectively. The nominal carbon concentrations are 10, 100, 500 and 1000 appm from left to right, where around

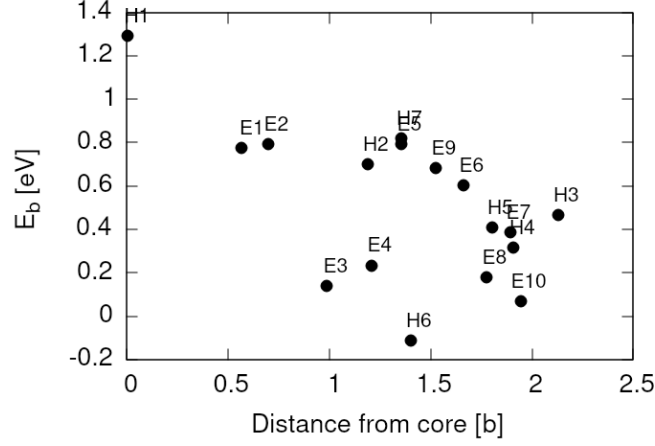


Fig. 11: Distance dependence of the binding energies of carbon to the  $1/2\langle 111 \rangle$  screw dislocation in iron. Positive binding energies denote a favourable binding.

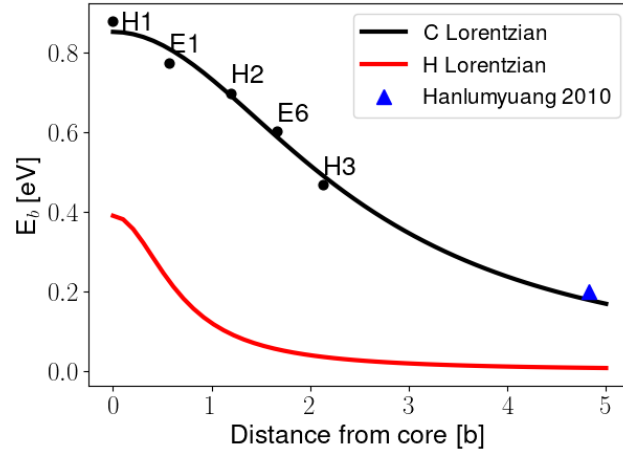


Fig. 12: Parameterised distance dependence of carbon binding energies to the  $1/2\langle 111 \rangle$  screw dislocation in iron. The sites chosen to fit to were determined by those sites a prismatic carbon in a hard core configuration would find itself, if the dislocation were to move without it along the  $X = \langle \bar{2}11 \rangle$  direction. The triangle, labelled Hanlumuayang, refers to the binding energy resulting from measurement of the elastic dipole tensor from DFT calculations evaluated at 12 [33]. Binding energy of hydrogen to the  $1/2\langle 111 \rangle$  screw dislocation also shown for comparison [20]

This distance-dependence agrees well with previous calculations of the binding energy at larger distances from the core [33].

#### 14.5.2 Kink-pair formation in pure iron

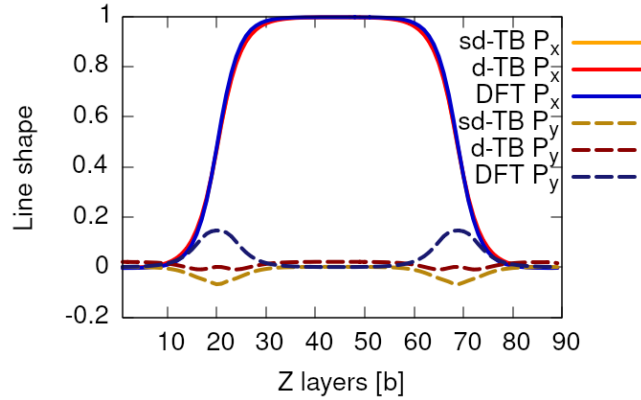


Fig. 13: Core positions of the line tension model from DFT (blue) and tight-binding (yellow) for the middle image corresponding to the MEP and the kink-pair formation energy. Images were relaxed using the ODE String method of Makri and Ortner [27].  $P_x$  and  $P_y$  correspond to the x/y-coordinate of the dislocation core position in each of the discretised layers of the dislocation. One finds that the kink width in tight-binding is wider than that found in DFT, which corresponds with the fact that the width is proportional to  $b\sqrt{K/\Delta E_P^{\text{tbe}}}$ , where the reduction in  $\Delta E_P^{\text{tbe}}$  is greater than the reduction in  $K^{\text{tbe}}$ .

In figure 13, one can see the  $P_x$  and  $P_y$  core positions which result from the highest enthalpy image of kink-pair formation for the canonical- $d$  and  $sd$  tight-binding models, where the DFT comparison is from [21]. Plots of the corresponding dislocation core pathway,  $P_j = (P_x^j, P_y^j)$ , looking down the dislocation line, are shown in 14.

The  $P_x$  line shape agrees well with the DFT-based results. The kink width was found to be slightly wider:  $W_k \sim 11b$  in tight-binding from the line-tension model, compared to  $10b$  in DFT and atomistic tight-binding results [30]. The larger width from tight-binding compared to DFT results from the width being proportional to  $b\sqrt{K/\Delta E_P}$  [21], with the discrepancy between the  $K^{\text{tbe}}$  and  $K^{\text{DFT}}$ , being smaller than that of the Peierls potential.

Differences in the  $P_y$  line shape are noticeable, with the canonical- $d$  model reproducing the result closest to the DFT  $P_y$  line shape.

The differences in line shapes manifest themselves clearly in plots of the dislocation pathway, figure 14, where we see the path a dislocation takes looking down the dislocation line. The core pathway dips below the midline in both the  $d$  and  $sd$  models, with a more pronounced effect being shown by the  $sd$  model. Apart from this discrepancy, we see there is good agreement between tight-binding to DFT when compared to the EAM potential of Mendeleev [?] in which we see a path which passes close to the split-core position. This is expected due to the low value of the Peierls potential of the EAM, as seen in figure 6.

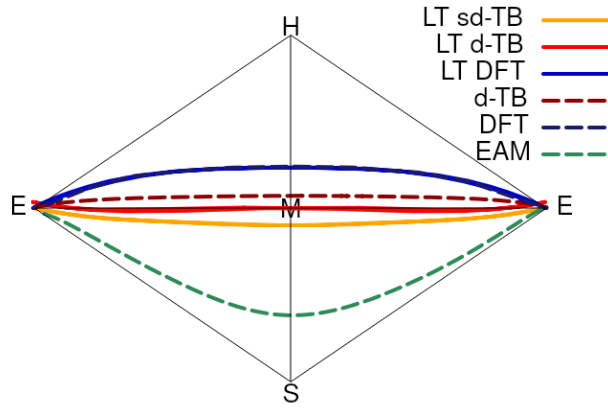


Fig. 14: Comparison of minimum energy pathways from different atomistic calculations to the line-tension model. Dashed lines correspond to atomistic calculations. Solid lines are results from the line-tension models. Tight-binding follows a pathway much closer to that of DFT. EAM potentials predict that the dislocation core goes to the split core and then back to the easy core. Even though the Peierls landscape found in tight binding has similar characteristics to the EAM in terms of the energetic ordering of different core states, the description of the minimum energy pathway of the  $1/2\langle 111 \rangle$  screw dislocation as it moves between core positions is in good agreement with DFT.

The kink-pair formation enthalpies obtained from the tight-binding models can be found in table 5. Tight-binding underestimates the kink-pair formation enthalpy by 0.18 eV, in comparison to DFT. This can largely be attributed to the difference in Peierls potentials between DFT and tight-

binding.

Table 5: Kink-pair formation energies between DFT, and the two flavours of tight-binding used with the line-tension model .

Method	$H_k$
DFT	0.71 eV
TB (sd-non-orthog.)	0.56 eV
TB (d-orthog.)	0.53 eV

### 14.5.3 Kink-pair formation enthalpy with a single carbon

To understand how kink-pair nucleation is affected by carbon, one can study the formation of a kink-pair but with the additional interaction of a single carbon ahead of the dislocation.

We place carbon in the E1 site, the highest binding energy site of carbon to the easy dislocation core. The carbon is fixed in place during kink-pair formation, as such we are assuming a regime in which the dislocation velocity is much greater than the diffusion of carbon. Carbon-dislocations interactions are only permitted between the dislocation segment closest to the carbon.

$P_x$  line shapes obtained during kink-pair formation can be seen in figure 15. The addition of carbon causes a cusp in the dislocation line towards the carbon in the initial and final images, due to the reduction in potential the central dislocation segment experiences due to carbon interaction. As the dislocation bows out to form a kink pair, the cusp becomes less prominent. As we reach the transition state, the dislocation image intersects the carbon position, to minimise energy.

The pathway corresponding to the highest enthalpy image, can be seen in figure 16. Looking along a direction, we see the path a dislocation takes in going between adjacent peierls valleys is asymmetric, as expected due to the due to the strong binding of carbon.

These features agree very well with the line tension model in Itakura [20], focussing on the case of dislocations undergoing kink-pair formation in the presence of a single hydrogen atom.

The kink-pair formation enthalpy of *sd* and *d* iron models, in both pure iron, and with carbon ahead of the dislocation line are shown in figure 17. The shape agrees well with results of the line tension model of Itakura [21], and from atomistic calculations of EAM [?] and GAP [?] Fe potentials. We find that carbon produces a consistent reduction of  $\sim 25\text{meV}$  to the kink-pair formation enthalpy when placed ahead of the dislocation line. The



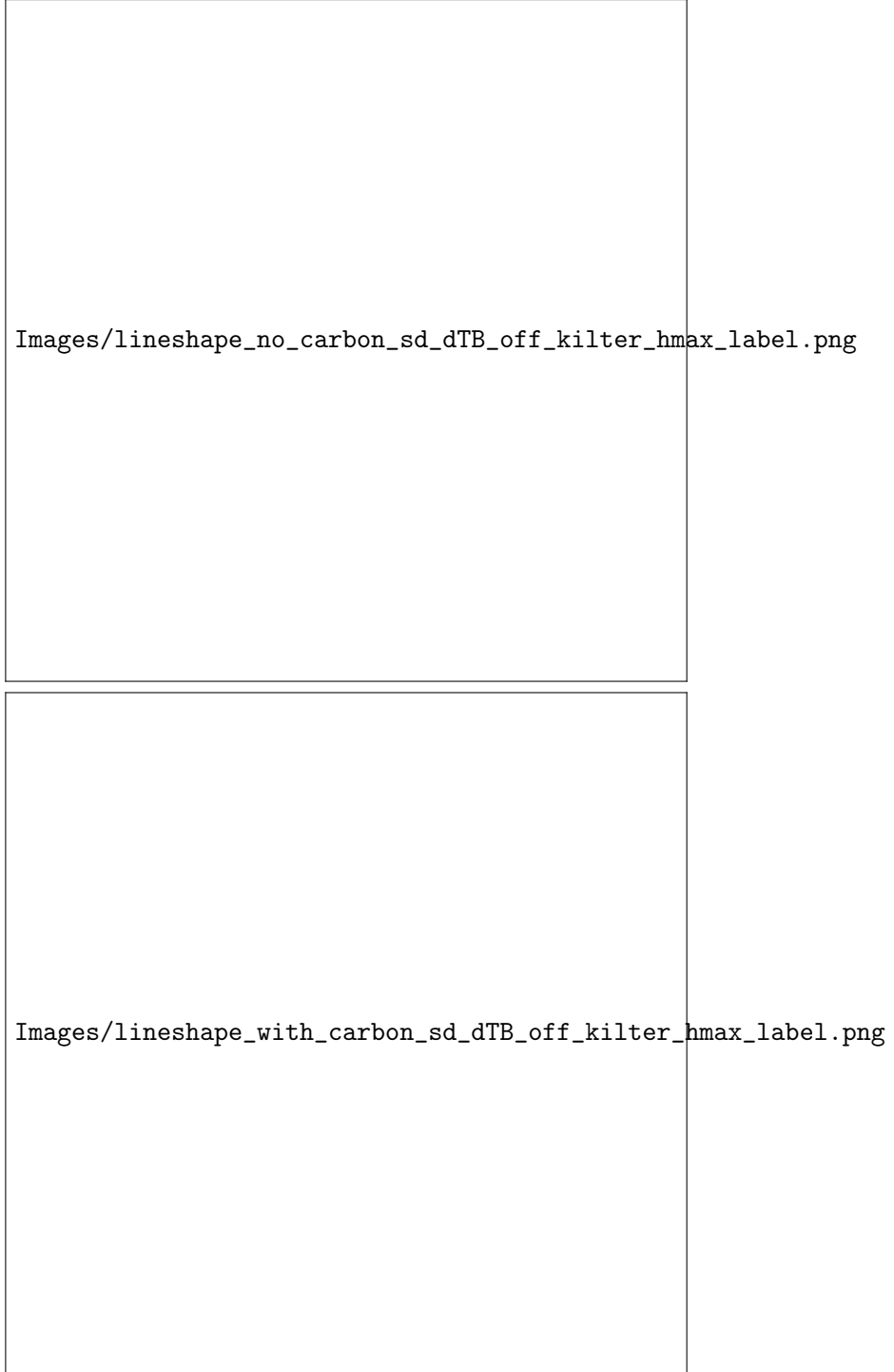


Fig. 15: Comparison of  $P_x$  lineshapes for the  $sd$  and  $d$  models in pure iron (top) and iron with a single carbon interacting with the central dislocation segment in E1 site (bottom). The highest enthalpy images,  $H_{\max}$ , for each of the models are shown in black. In pure iron, the  $d$  model lineshapes are offset from the  $sd$  due to the different Peierls potentials involved. With carbon along the path of migration, we find the dislocation intersects the solute, due to its large binding energy.

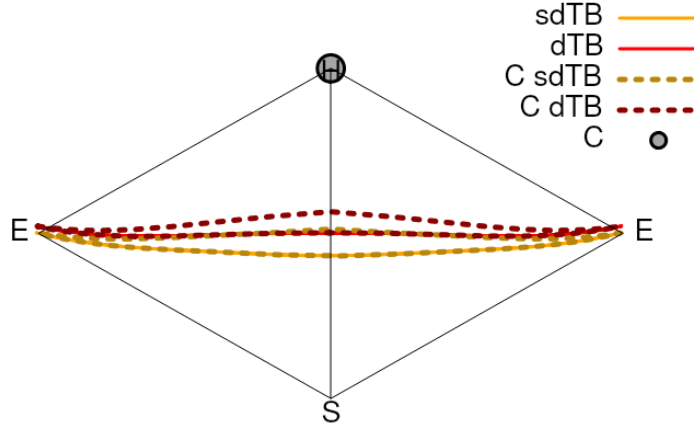


Fig. 16: The migration path of the highest enthalpy images for both the *sd* and *d* tight-binding models with a single carbon in an E1 site. Carbon causes a deviation of the kink-pair formation path from the pure iron case (solid lines), due to carbon-dislocation binding.

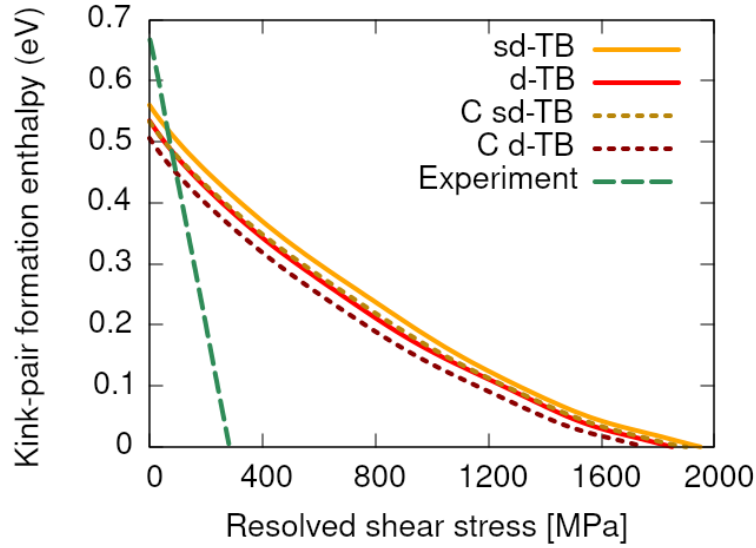


Fig. 17: Dependence of the kink-pair formation enthalpy with increasing stress on the  $[111](\bar{1}\bar{1}0)$  direction. Solid lines: pure iron. Dotted lines: carbon ahead of the dislocation line in an octahedral site. Experimental data taken from Spitzig [34].

reduction is surprisingly small compared to the effect of hydrogen interaction with dislocations [20], which gives a reduction of  $\sim 110\text{meV}$ . The discrepancy between carbon and hydrogen is due to the more gradual decrease of the carbon-dislocation interaction—over the distance between the initial and transition states—compared to the hydrogen-dislocation interaction, as shown in figure 12. Comparing the two interaction functions, we have at the Peierls valley  $P_{\text{disl}} = (0, 0)$ , and  $P^{\text{H}} = P^{\text{C}} = (1.17, 0.68)$  giving a distance  $d = 0.54b$  between the dislocation and the solute. The difference in the interaction energy for a dislocation segment in the final position in interaction for hydrogen  $\Delta E_b^{\text{H}} = E_b(\text{H}, 0) - E_b(\text{H}, 0.54b) = 150\text{ meV}$ , whereas for carbon we have  $\Delta E_b^{\text{C}} = E_b(\text{C}, 0) - E_b(\text{C}, 0.54b) = 40\text{ meV}$ .

Due to the longer range of the interaction function, we expect that a single carbon will provide comparable decreases to the kink-pair formation up to distances up to  $5b$ , if placed ahead of the dislocation line. At equilibrium, where carbon exhibits long-range ordering along the dislocation line in the H1 and H2 sites [?], we can expect a decrease in the kink-pair formation enthalpy. Line-tension simulations in ordered carbon environments are necessary to account for this properly. We can approximately treat some of these effects using an effective carbon-dislocation interaction along the dislocation line during kink-pair formation, as shown in section 14.6.2.

The stress at which the kink-pair formation enthalpy becomes zero is the Peierls stress. In the zero temperature limit, we can approximately account for quantum effects, such as tunnelling and zero-point energy, by subtracting the Wigner correction, determined by quantum transition state theory [?, ?], from the kink-pair formation enthalpy. Calculating this correction within atomistic tight-binding simulations is currently intractable. The correction has been calculated using the Mendelev EAM potential [?] for a screw dislocation undergoing kink-pair nucleation [?]. The Wigner correction obtained is  $0.09\text{eV}$ . We find that the Peierls stress obtained for both the  $sd$  and  $d$  models is  $\approx 1.2\text{GPa}$ , see table 6.

Discrepancies in the kink-pair formation enthalpy compared to experimental measurements of Spitzig [34], can be attributed to multiple sources. In bcc metals, experimental measurements of the CRSS, which can be linked to the kink-pair formation enthalpy, are thought to measure the stress required to operate Frank-Read sources which have been blocked due to the back stress of generated screw dislocations [?]. As mixed dislocations bow out from the source, long screw segments form—due to the higher mobility of mixed/edge character segments compared to screw segments. Between the source and the screw dislocations, there are non-screw dislocations, stresses from which act in conjunction with applied stress to reduce the necessary

Table 6: Peierls stress of screw dislocation taken from the line tension model with the effect of the correction to the Peierls stress from quantum effects, estimated by Provile [?]. DFT results are found from papers of Itakura and Krach [21, ?], where Itakura *et al.* used a DFT-derived line-tension model, and Kraych used DFT NEB calculations. \* corresponds to use of Itakura DFT data in this implementation of the line-tension model.

Model	Peierls Stress [GPa]	Peierls Stress with Wigner correction [GPa]
sd-TB	1.95	1.35
C sd-TB	1.90	1.30
d-TB	1.85	1.30
C sd-TB	1.75	1.20
DFT [Kraych, 2019]	2.00	
DFT [Itakura, 2012]	1.00 [*2.10]	

CRSS by 2-3 times. As such the enthalpy barrier obtained from the experimental CRSS measurements of Spitzig, cannot be directly compared to the true kink-pair formation enthalpy necessary for a single screw dislocation to undergo thermally-activated movement.

#### 14.5.4 Kink-pair nucleation rate

One can use an Arrhenius law to calculate the attempt frequency of a process given an energy barrier  $E_{\text{barrier}}$  [?],

$$\nu(E_{\text{barrier}}, T) = \nu_0 \exp\left(-\frac{E_{\text{barrier}}}{k_B T}\right), \quad (8)$$

where  $\nu_0$  is an initial attempt frequency.

The kink-pair nucleation rate of a dislocation of length  $N_d$  burgers vectors is given as [20]:

$$\nu_d = \nu(H_k(\sigma), T) N_d, \quad (9)$$

where  $H_k(\sigma)$  is the kink-pair formation enthalpy. Experimental results of *in situ* straining of Fe from Caillard [?], enable calculation of the attempt frequency for stable kink-pairs: assuming  $b = 2\mu\text{m}$ ,  $T = 300\text{K}$  and an applied stress of  $33\text{MPa}$  one obtains  $\nu_d = 81\text{s}^{-1}$ .

There will be an enhancement of the rate due to carbon occupying sites ahead of the dislocation. Given a concentration of carbon on the dislocation line,  $c_d$ , we have in the sites ahead, the rate enhancement factor is

$$f_r(c_d, \Delta H_k, T) = 1 + c_d W_k \{\exp(\Delta H_k / k_B T) - 1\}. \quad (10)$$

where  $\Delta H_k = H_k - H_k^C = 25\text{meV}$  and  $W_k \sim 10b$  is the kink-width. Assuming  $T = 300\text{ K}$ , and assuming the concentration of carbon is  $c_d^{E2}$ , we obtain enhancement factors as shown in table 7.

Table 7: Enhancement factors to the kink nucleation rate and corresponding critical temperatures.  $c_d$  was taken as the value reached from self-consistency at  $T=300\text{K}$ , at a dislocation density of  $\rho = 10^{15}$ , as seen in figure 10. Kink-pair nucleation rate enhancements steadily increase until concentrations at which all dislocations are decorated with carbon, in the cases of  $C_{\text{nom}} \geq 500$  appm. The critical temperatures are all well above operating temperature, so we can expect rate enhancements during operation.

$c_{\text{nom}}$ [appm]	$f_r$ , Rate Enhancement factor	$T_U$ [K]
10	4.4	745
100	7.9	1329
500	17.3	3043
1000	17.3	3043

These rate enhancements are an order of magnitude less compared to what one finds with hydrogen in iron [30], due to the small reduction to the kink-pair formation enthalpy with carbon. However, this only accounts for the effect of a single carbon just ahead of the core. Complex ordering phenomena of carbon has been found along the screw dislocation in Fe, which could enhance the kink-nucleation rate [?]. Ising models parameterised on *ab-initio* data give equilibrium concentrations of different carbon trap sites along the dislocation core, accounting for carbon-carbon repulsion. They predict H1 and H2-type sites in adjacent layers can have concentrations which are  $\sim 1.0$  and  $\sim 0.25$  respectively, when the nominal carbon concentration is 100 appm. The effect of multiple carbon-dislocation interactions on the the kink-pair formation enthalpy has yet to be determined, but we expect  $\Delta H_k$  and therefore the rate enhancement, to increase.

Significant enhancement of the nucleation rate occurs when the rate enhancement factor is on the order of  $f_r \sim 1$  or greater. Defining  $c_d^E = \frac{1}{W_k \{\exp(\Delta H_k / k_B T) - 1\}}$ , one can impose a condition when  $c_d^E > c_d$ , defining a critical temperature  $T_U$  after which these enhancements are not deemed important. See table 7. All the critical temperatures are found to be above operating temperature.

The diffusion coefficient of carbon in bcc Fe has been calculated in DFT

as  $D_C = 1.44 \times 10^{-7} \text{m}^2 \text{s}^{-1}$ , which agrees well with experiment [?, ?]. The attempt frequency is related to the diffusion coefficient by  $\nu_0 = 6D_0/a^2$  [?], which gives the attempt frequency of carbon as  $\nu_C^0 = 1.0 \times 10^{13} \text{s}^{-1}$  [28]. The migration energy barrier of carbon in bcc Fe was found to be  $E_C^{\text{m bulk}} = 0.87 \text{eV}$  in DFT calculations.

From the experimental rate of stable kink-pair nucleation  $\nu_d = 88 \text{s}^{-1}$  from Caillard, we can estimate the prefactor  $\nu_d^0 = 0.99 \times 10^8 \text{s}^{-1}$  using experimental the kink-pair formation enthalpy at 33 MPa [20].

The average velocity associated with a process undergoing thermal activation of a barrier is given by  $\bar{v} = d_{\text{barrier}}\nu$ , where  $d_{\text{barrier}}$  is the distance between the the initial and final states of the barrier. For dislocations we use  $d_d = a\sqrt{2/3}$  is the distance between Peierls valleys for kink-pair formation and  $d_C = 1.2$  is the distance between octahedral sites which carbon can jump to. As these distances are on the same order of magnitude, we omit the explicit calculation of velocities for clarity, using the attempt frequencies for comparisons.

At  $T = 300 \text{K}$  and  $C_{\text{nom}} = 1000 \text{appm}$ , around the solubility limit of carbon in ferrite (0.02 wt% C), we have  $\nu_C(E_C^{\text{m bulk}}, 300) = 2.4 \times 10^{-2} \text{s}^{-1}$ , with  $f_r(1000 \text{appm})\nu_d(H_k, 300) = 1.7 \times 10^{-1} \text{s}^{-1}$ . This shows that in the bulk, carbon cannot be assumed to move with the dislocation, as the attempt frequency of carbon is an order of magnitude less than that of kink-pair formation.

However, it has been shown in EAM calculations that much lower carbon migration barriers exist in the vicinity of a screw dislocations [28]. The migration barrier of carbon is reduced to  $E_C^{\text{m disl.}} = 0.2 \text{eV}$ . Using this value we obtain  $\nu_C(E_C^{\text{m disl.}}, 300) = 4.4 \times 10^9 \text{s}^{-1}$ . We see that the average carbon velocity will be much greater than that of dislocations undergoing thermally-activated movement, as such we can assume that in the high-mobility zone, that carbon is able to move with dislocations.

The timescale of carbon redistribution with dislocation movement remains negligible as long as the kink-pair formation enthalpy with carbon  $H_k^C(\sigma)$  is greater than the migration barrier energy in high mobility zone:  $H_k(\sigma) - \Delta H_k^C(\sigma) > E_C^{\text{m}}$ . Using this value, we can obtain an upper critical stress  $\sigma_c^{\text{U}} \sim 210 \text{MPa}$ , above which carbon cannot enhance dislocation mobility, as it cannot catch up with the dislocation.

#### 14.5.5 Kink-trapping

Kink-trapping is the energetic barrier to kink-migration along the dislocation line due to the change in binding energy of a kink sweeping past a defect.

The kink-trapping effect due to carbon can be estimated as follows [20]. If a kink-pair were to form with a carbon in an E1 site behind the dislocation, the carbon-dislocation binding energy will change. We can assume carbon remains in its site upon movement: the barrier to kink-migration has been shown to be small [20, 30, ?], as such kink-migration is orders of magnitude faster than that of carbon diffusion.

As the kink sweeps past, the E1 site becomes an E6 site, resulting in a difference in binding energy of  $\Delta E_b^{E1 \rightarrow E6} = 0.775 - 0.603 = 172$  meV. This trapping effect is expected to decrease with applied stress, as shown in Itakura, but this is left for future work.

The kink-trapping effect of carbon will be pronounced when a dislocation moves from its equilibrium position as there will be multiple carbons along the dislocation line [?]. This effect has yet to be estimated.

This is an important effect to account for, as solute drag has been shown to reduce the kink-migration velocity sufficiently such that jogs can form on dislocations due to the collision of kinks on different glide planes causing pinning and the formation of edge dipoles seen in experiment [?, ?].

## 14.6 Line-tension equilibrium conditions

### 14.6.1 Dynamics of straight $1/2\langle 111 \rangle$ screw dislocation

Figure 18 shows the potential a straight screw dislocation experiences as it moves between peierls valleys in an equilibrium carbon environment, allowing carbon to redistribute between trap sites upon glide. The potential a dislocation experiences decreases as carbon concentration is increased. This is due to the stabilisation of the hard core position with increases in carbon content. With stabilisation, E1/2 sites are distorted into H1 sites. At concentrations 20appm, the mean carbon-dislocation interaction energy becomes greater in magnitude than the bare Peierls potential, resulting in a potential well.

Figure 19 shows the case where the concentration of carbon is not allowed to equilibrate: simulating the limit of rapid glide, where the occupancies of carbon in all trap sites is fixed to the value determined at the initial easy-core configuration of the straight dislocation. The occupancies decrease rapidly with distance from the core. As such, the energy a straight dislocation experiences, relative to the initial dislocation position, increases with distance from the Peierls valley, due to a reduction in the dislocation-carbon interaction energy from a lack of carbon occupancy.

In reality, we have a situation which is between the two. This can be

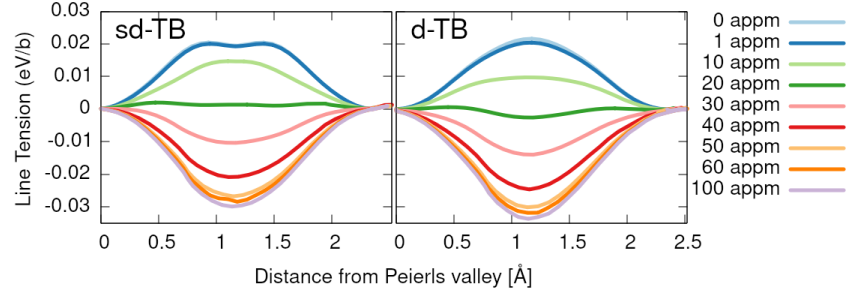


Fig. 18: Enthalpies of straight screw dislocation in the line-tension model in an environment of carbon with concentrations determined by thermodynamical mean field model. Carbon concentration on the dislocation on the dislocation line is in equilibrium with the bulk according to the concentration given by the H1 site, where carbon is able to redistribute between the sites according to Maxwell-Boltzmann statistics.

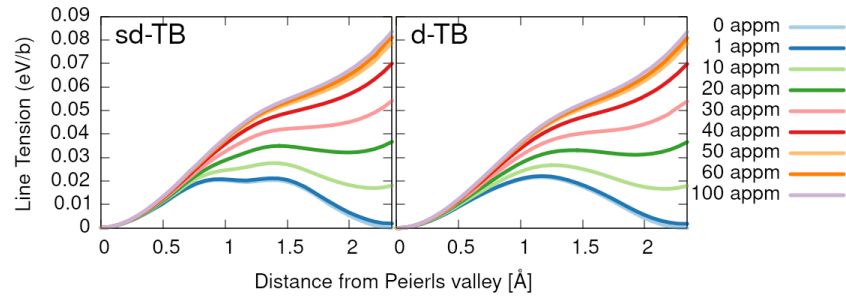


Fig. 19: Enthalpies of straight screw dislocation in the line-tension model in an environment of carbon with concentrations determined by thermodynamical mean field model. Concentration of carbon in each of the sites is fixed to its initial value, simulating the limit where carbon does not have time to equilibrate with dislocation movement.



accounted for by a continuity term which is dependent on dislocation velocity [?].

#### 14.6.2 Dynamics of kink-pair formation in equilibrium

The line-tension upon kink-pair formation, in the limit of slow glide, can be seen in figure 20. As the hard core is stabilised with increasing carbon content, the line tension decreases, due to the negation of the bare Peierls potential with increasing carbon-dislocation interaction energy. At nominal concentrations greater than 20 appm, the string method finds lower energy dislocation configurations away from the straight initial easy core position favoured at lower concentrations.

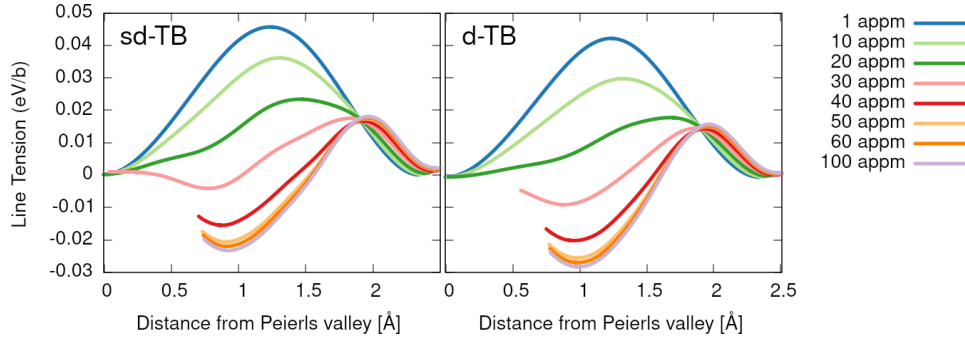


Fig. 20: Enthalpies of the maximum enthalpy images upon kink-pair formation with increasing carbon content. Carbon interaction causes a reduction in the enthalpy barrier as due to the negation of the effect of the bare Peierls potential. As the nominal carbon concentration passes 20 appm, the hard core is stabilised, thus causing the string method algorithm to find a global minimum closer to the hard core position.

With increasing carbon concentration, both tight-binding models exhibit a deviation of the maximum enthalpy pathway towards the hard core, as shown in figure 21. At each concentration, the path a dislocation takes in the  $d$  tight-binding model is closer to the hard core, due to the morphology of its peierls potential.

The lineshapes of the  $P_x$  dislocation coordinate on kink-pair formation broaden with carbon content due to the attraction of the dislocation line to carbon sites.

The kink-pair formation enthalpy in an effective carbon concentration can be seen to decrease with increasing carbon content. At concentrations

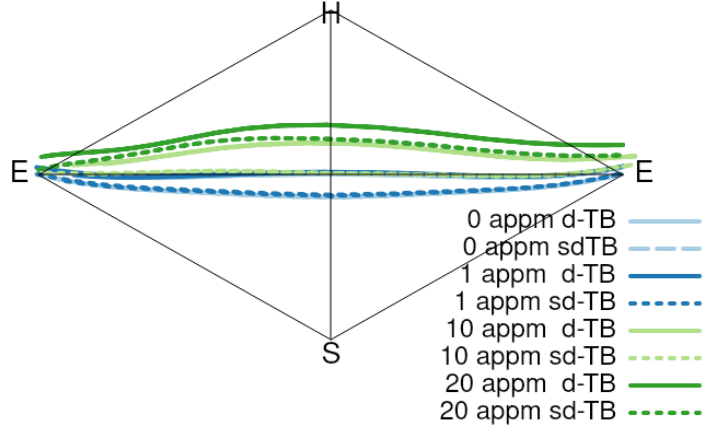


Fig. 21: Maximum enthalpy pathways found upon kink-pair formation in an environment of carbon for both tight-binding models at different nominal carbon concentrations. Concentrations shown are before the easy core becomes unstable. With an increase in carbon content, path starts to deviate towards the hard core.

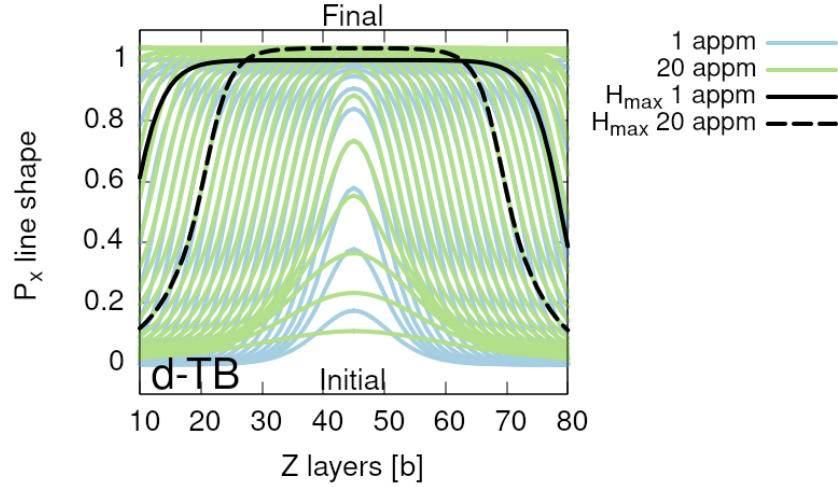


Fig. 22:  $P_x$  lineshape comparison of differing concentrations of the canonical- $d$  tight-binding model.

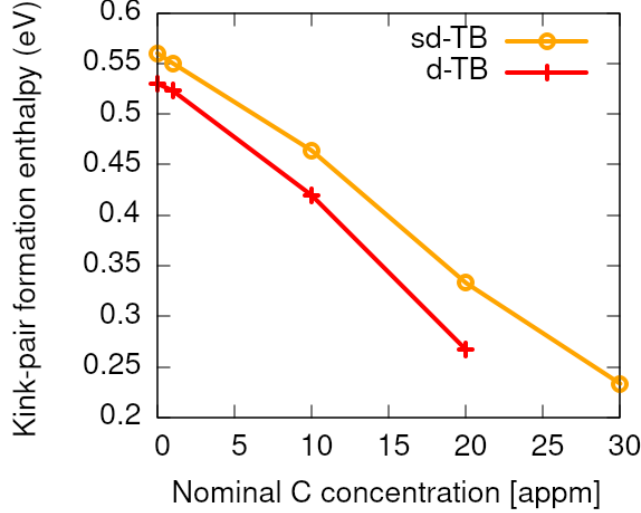


Fig. 23: Kink-pair formation enthalpy dependence on nominal carbon concentration without the application of stress. There is a consistent decrease in the mean kink-pair formation enthalpy with carbon content.

greater than 20 appm, the hard core is stabilised. Line-tension calculations of the kink-pair formation of a dislocation moving from the stabilised hard core to an adjacent hard-core position are necessary to ascertain the kink-pair formation enthalpy at higher carbon contents. We expect, as was seen in self-consistent calculations of the kink-pair formation enthalpy in hydrogen, that the trend will be reversed: the kink-pair formation enthalpy will increase with carbon content, once the hard core has been stabilised.

One can see the effect that these mean enthalpies have on the kink-pair nucleation rate. Using the results of the kink-pair formation enthalpy from the canonical- $d$  tight-binding model, and using equations (9) and (8) we have the rates as shown in table 8. The rate enhancement factor is not included here as the concentration term is taken into account in the kink-pair formation calculation itself.

Table 8: Kink-pair nucleation rate in an environment of carbon using the results of the canonical  $d$ -band model, using from equations (9) and (8)

$c_{\text{nom}}$ [appm]	$\nu^d$
10	8.7
20	2881.8

Allowing carbon to equilibrate between trap sites during kink-pair formation, we see a large enhancement to the kink pair nucleation rate, increasing dislocation velocity. Carbon remains with screw dislocations upon movement, due to the low barrier to migration in the high-mobility zone resulting in a velocity orders of magnitude greater than that of dislocation motion. The analysis shown here is approximate. A more complete description necessitates a self-consistent treatment of the kink-pair formation enthalpies, as  $H_k = H_k(\bar{v}_d)$  and  $\bar{v}_d = \bar{v}_d(H_k)$ . This is left for future work.

## 14.7 Diffusion Barriers

The diffusion barriers of carbon close to the easy core have been found to decrease—for some transitions—from 0.87eV for bulk diffusion, down to barriers around 0.2eV [28]. In the calculations shown in section 14.5.4, we see that carbon is able to keep up with the dislocation in a range of moderate velocities only if this diffusion barrier is lowered to such a level.

However, the predictive power of the EAM potential used to obtain these barriers is limited. The Mendelev EAM potential used in these calculations is unable to reproduce: the 2D Peierls potential, which is double-humped, instead of single-humped [?]; the metastable hard core structure, which exhibits a spontaneous reconstruction to the hard core from the easy core and, the binding energies of carbon close to the dislocation core—being roughly half that found in Ventelon and this work [32, 19]. These discrepancies are likely due to the inherent lack of quantum mechanics in the EAM description of bonding, which seems necessary for an accurate description of energetics close to the dislocation core. As such, it remains to be seen if the diffusion barriers, and consequent diffusion rates obtained from this EAM potential are faithful.

As seen in figure 10, at moderate dislocation densities, we expect all dislocations to be decorated with carbon, and be of hard-core type. As such, it is important to ascertain the diffusion barriers of carbon around the hard core, as it is the core we expect to find most commonly in iron. From this, we can ascertain if there exists a high-mobility zone around dislocations in bcc iron, validating the EAM results of Nematollahi and the Fe-C potential of Becquart [28, 32].

### 14.7.1 Theory

Using the diffusion barriers, we can find useful quantities, such as diffusion coefficients for each of the carbon sites around the hard core of the disloca-

tion.

We follow the method detailed in the calculations of Lu *et al.* [?]. The diffusion coefficient is given by

$$D = D_0 \exp(-E_a/kT)$$

where  $D_0$  is a prefactor, and  $E_a$  is the activation energy. This can also be equivalently expressed as

$$D = n\beta d^2 \Gamma,$$

where  $n$  is the number of nearest neighbour stable sites for the diffusing atom,  $\beta$  is the jump probability in the direction of diffusion,  $d$  is the length of the jump directed in the direction of diffusion and  $\Gamma$  is the jump rate between adjacent sites of the diffusing atom.

The jump rate is given by the equation,

$$\Gamma = \frac{kT}{h} \frac{\prod_{i=1}^{3N-6} [1 - \exp(-h\nu_i^0/kT)]}{\prod_{i=1}^{3N-7} [1 - \exp(-h\nu_i^*/kT)]} \exp(-\Delta H_m/kT)$$

Where we have the  $i^{\text{th}}$  normal mode frequency of the initial and saddle point images as  $\nu_i^0$  and  $\nu_i^*$ , respectively, where  $\Delta H_m$  is the difference in enthalpies between the saddle point and the initial image.

Can alternatively find  $\Gamma$  by obtaining the phonon free energy of a given image,

$$F_{\text{vib}} = kT \int_0^\infty g(\nu) \ln \left[ 2 \sinh \left( \frac{h\nu}{kT} \right) \right] d\nu$$

and so the jump rate can be expressed as

$$\Gamma = \frac{kT}{h} \exp[-\Delta F_{\text{vib}} + \Delta H_{(m)} / kT]$$

The zero point energy is included in the vibrational term.

Included in this is the assumption that using the harmonic approximation is valid throughout this. However for accurate elucidation of effects at finite temperature, anharmonicity must be included.

### 14.7.2 Computational Method

Elucidation of the diffusion barriers of carbon, was achieved using the Climbing-Image Nudged Elastic Band (CI-NEB) method with either 5 or 9 images. Fully-relaxed cluster simulation cells of dislocation-carbon interactions, as

detailed above, were used for the initial and final images. Intermediate images were initially determined by a linear interpolation between the two. The same k-point mesh,  $1 \times 1 \times 12$  was used. The images were relaxed until all forces were below  $20 \text{ meV}^{-1}$ . To prevent rotations and translations [?], six degrees of freedom were fixed for each image. The CI-NEB algorithm allows for the highest energy image to climb, by simply neglecting the spring forces acting on the image. This gives the true saddle point. Restoring forces were checked for each of the highest energy images.

The difference in vibrational free energies between cells comes from the difference in carbon placement from the initial images. One expects only significant changes the force constants calculated from the displacement of an atom close to the carbon defect. This implies that a good approximation to the true phonon free energy difference can be calculated using a subset of the original cell. This would further decrease the computational time necessary to obtain the vibrational free energy.

To facilitate the vibrational free energy calculations, we use the **phonopy** package [?]. With the addition of the defect in the cell, there is no symmetry to reduce the computational cost. This necessitates the displacement of each atom three times, for each degree of freedom. To reduce the computational cost, we allow **phonopy** to generate displacements from a smaller cell of radius  $R = 3\sqrt{2}a_{\text{bcc}}$ , cut out from the dynamic region. We assume here that the extra vibrational modes which arise from the omitted part of the computational cell will have a negligible effect on the difference in free energies, and thus the jump rate. The displacements generated are applied to the original cell and a calculation of the forces, under self-consistency to a charge tolerance of  $1e-6$ , is performed. The forces acting on particular atoms are extracted and fed into phonopy, from which we obtain the vibrational free energy.

### 14.7.3 Enthalpies in dislocation movement with static carbon

The change in Gibbs free energy between differing configurations of a dislocation-carbon system can indicate favourable transitions, resulting in potential mechanisms for dislocation-assisted carbon migration. For example, consider a dislocation going from the hard to the easy core, with carbon segregated to the core in particular sites. If the Gibbs free energy difference is less than zero, we can regard the change as favourable for the system. This allows us to search for potential mechanisms which allow carbon to move with the dislocation. Assuming the whole dislocation line moves at once, and neglecting the energy difference arising from the slightly different elastic

dipole tensors generated from the different environments of carbon around each core, from equation 13.5 we have the change in enthalpy as

$$\Delta H_{\text{LT}}(\sigma) = \Delta H_{\text{core 1} + \text{C}\alpha \rightarrow \text{core 2} + \text{C}\beta} = \Delta E_{\text{core}}^{1 \rightarrow 2} + (\sigma \cdot \vec{b}) \times \vec{l} \cdot (\Delta \vec{P}_{\text{core}}) - \Delta E_{\text{b}}^{\text{C}\alpha \rightarrow \text{C}\beta}, \quad (11)$$

where  $\alpha$  and  $\beta$  are indices for different carbon binding sites of core 1 or core 2,  $\Delta \vec{P}_{\text{core}}$ , is the change in core position of the dislocation and  $\Delta E_{\text{core}}^{1 \rightarrow 2}$  is the difference in energy between the cores.

The change in the Gibbs free energy is given by

$$\Delta G(T, \sigma) = \Delta H(\sigma) - T\Delta S = \Delta H_{\text{LT}}(\sigma) + \Delta F_{\text{vib}}(T, V) + \Delta F_{\text{conf}}(T, V).$$

We neglect electronic and magnetic contributions to the free energy, and assume constant volume.

The vibrational contribution to the free energy can be obtained by calculation of the phonon density of states, as done by calculations by **phonopy**. Considering only those binding sites sampled close to the core, there are up to six equivalent sites for carbon around the core, due to the three-fold rotational symmetry about the dislocation core in addition to three  $C_2$  point groups with rotation axes at 30 deg, 90 deg and 120 deg, as measured from the  $x$ -axis, as seen in figure 9. The configurational entropy therefore has a maximum magnitude of  $S_{\text{conf}} = k_{\text{b}} \ln(\Omega) = k_{\text{B}} \ln(6)$ , as such we can say the change in configurational entropy is negligible, due to the magnitude of the Boltzmann constant causing it to be orders of magnitude less than the other terms. Therefore we obtain

$$\Delta G = \Delta E_{\text{core}}^{1 \rightarrow 2} + \Delta F_{\text{vib}} + (\sigma \cdot \vec{b}) \times \vec{l} \cdot (\Delta \vec{P}_{\text{core}}) - \Delta E_{\text{b}}^{\text{C}\alpha \rightarrow \text{C}\beta} \quad (12)$$

In going from the hard core to the easy core, we have:

$$\Delta G_{\text{d. hard} + \text{C}\alpha \rightarrow \text{d. easy} + \text{C}\beta} = -\Delta E_{\text{core}}^{\text{Easy-Hard}} + (\sigma \cdot \vec{b}) \times \vec{l} \cdot (\vec{P}_{\text{hard}} - \vec{P}_{\text{easy}}) - \Delta E_{\text{b}}^{\text{H}\alpha \rightarrow \text{E}\beta} \quad (13)$$

$$= -40\text{meV} - \sigma_{yz} \cdot \frac{\sqrt{3}}{2} a_{\text{bcc}} + \Delta F_{\text{vib}} - \Delta E_{\text{b}}^{\text{H}\alpha \rightarrow \text{E}\beta} \quad (14)$$

$$\therefore \quad \text{if} \quad \Delta F_{\text{vib}} < 40\text{meV} + \sigma_{yz} \cdot \frac{\sqrt{3}}{2} a_{\text{bcc}} + \Delta E_{\text{b}}^{\text{H}\alpha \rightarrow \text{E}\beta}$$

then the change is favourable.

at zero stress, we have

$$\Delta E_{\text{core 1} + \text{C}\alpha \rightarrow \text{core 2} + \text{C}\beta} = \Delta E_{\text{core}}^{1 \rightarrow 2} - \Delta E_{\text{b}}^{\text{C}\alpha \rightarrow \text{C}\beta} \quad (15)$$

If this energy change,  $\Delta E_{\text{core 1} + \text{C}\alpha \rightarrow \text{core 2} + \text{C}\beta}$  is negative, then one can assume that this is a favourable process, and the difference in enthalpy is available for the activation of a diffusion barrier. We can think of the second term, as the work done by the dislocation against the external stress field to move to an adjacent core position. In general, the stress tensor used should incorporate the stress due to the tetragonal distortion of the carbon as well as applied stress. We do not incorporate this effect in this analysis.

1. Caveats for the calculation of the vibrational free energy on a subsection of lattice

In doing the phonon calculations on a subset of the simulation cell, one assumes here that the force constants generated are not long-ranged. To properly analyse this, one can analyse the properties of the force constants using the Hellman-Feynman theorem and linear response theory [35].

It was shown by Pettifor and Finnis [?] in Finnis-Sinclair models that the magnitude of the force constants, out to more than six shells of neighbours, depends strongly on the band structure and the value of the Fermi energy, and does not fall off rapidly or even monotonically with distance.

There are other approximations to calculating the change in the free energy: the Debye model, or the local harmonic model [?].

#### 14.7.4 Modification of occupancies due to diffusion barrier

To model the solute atmosphere around a dislocation in an environment of carbon, which is allowed to diffuse, we can use a discrete diffusion model, as detailed in Yoshinaga [36]. Applying harmonic transition-state theory to the migration of carbon to adjacent sites around each of the cores, we are able to ascertain the energy barriers, and therefore the rates of carbon diffusion around each of the cores, from which we can determine the evolution of carbon concentration with time. Nematollahi *et al.* [28] extended this model to include the effect of changes in occupancy upon dislocation movement.

The total change in occupancy can be described by the equation



$$\frac{\partial \chi_i}{\partial t} = \sum_{j=1}^4 \left\{ \chi_j (1 - \chi_i) \nu_0^{\text{migration}} \exp \left[ -E_{\text{barrier}}^{i \rightarrow j} / k_B T \right] - \chi_i (1 - \chi_j) \nu_0^{\text{migration}} \exp \left[ -E_{\text{barrier}}^{j \rightarrow i} / k_B T \right] \right\} + \frac{\bar{v}_{\text{disl}}}{a/2} [\chi_{j+} - \chi_i],$$

where  $\chi_i$ , is the occupancy of a particular carbon site,  $E_{\text{barrier}}^{j \rightarrow i}$ , is the migration barrier of carbon from site  $j$  to site  $i$ ,  $\nu_0$  is the attempt frequency. The summation is over the four nearest sites available for carbon to diffuse to. The last term in equation (??), is a convection term, allowing concentrations to change upon a dislocation moving with average velocity  $\bar{v}_{\text{disl}}$ . We use the convention of a dislocation moving along the positive  $x$ -axis; as such,  $\chi_{j+}$  is the occupation of a site to the right of site  $i$  the dislocation, which is biased to move towards the  $\chi_i$  upon dislocation movement, and similarly site  $i$  will move the the  $j$ - site, to the left of the dislocation.

In the paper of Gong *et al.* [?], the diffusion model has a different form. The occupancy of carbon is taken as a proportion of the difference between the limiting cases of dislocation movement: slow dislocation movement, where carbon is able to equilibrate with the dislocation, and fast dislocation movement, where carbon occupancies are fixed. This has the form of

$$\frac{\partial \chi_i}{\partial t} = \bar{v}_{\text{disl}} \frac{\partial \chi_i}{\partial x} = (\chi_i^e(x) - \chi_i(x, \bar{v})) \nu_0^{\text{solute escape}} \exp -E_i(r) / k_B T,$$

where  $\chi_i^e$  is the equilibrium occupancy of site  $i$ ,  $\chi_i$  is the true occupancy of the site, which is solved for,  $\nu_0^{\text{solute escape}}$  is the attempt frequency for carbon to escape the solute atmosphere, and  $E_i(r)$  is the *binding* energy of carbon to the  $i^{\text{th}}$  site, which has been parameterised by a dependence on the distance from the dislocation core  $r$ . This equation can be solved self-consistently with

$$\bar{v}_{\text{disl}}(H_k) = h \nu_k^0 \exp(-H_k(C_C, \sigma, \bar{v}_{\text{disl}})),$$

where  $h = a\sqrt{2/3}$  is the distance between two Peierls valleys,  $\nu_k^0 = 2.31 \times 10^9 \text{s}^{-1}$  is the attempt frequency for stable kink-pair formation and  $H_k$  is the kink-pair formation enthalpy at a given carbon concentration, stress and average dislocation velocity.

- In Ivo's paper, the change in occupancy has a time dependence, which is due to the velocity of a dislocation.

- This mediated between the two limiting regimes of static and equilibrium occupancies upon dislocation motion.

$$\frac{\partial \chi_i}{\partial t} = \bar{v} \frac{\partial \chi_i}{\partial x} = (\chi_i^e(x) - \chi_i(x, \bar{v})) \nu_0^{\text{solute escape}} \exp -E_i(r)/k_B T$$

- Here the attempt frequencies are different as one is for a hydrogen to escape from the binding of the dislocation to the bulk, and the other is to escape the relative energy barrier between sites.
- If it is possible to assume that one can superimpose the occupancy effects of carbon diffusion, then we can have an equation for the velocity dependence.

## 15 Discussion

The Peierls potential is reproduced well by tight-binding. For a Peierls potential more reminiscent of finite temperature materials, one could have given a more thorough treatment of magnetism. All calculations were performed at 0 K, using the ferromagnetic ground state of iron during dislocation relaxations. One could have performed multiple dislocation relaxations using the noncollinear disordered local moment approximation to handle paramagnetism, as was achieved by Casillas and Ventelon [?]. Their calculations showed that the energy difference between the hard and easy cores is lowered to  $26 \pm 20 \text{ meV}/b$ , from  $40 \text{ meV}/b$ . The error bars are too large to confirm the hypothesis that the Peierls potential is significantly different, and the tight-binding results coincidentally fall exactly into the middle of their range. As such, the resultant Peierls potential from ferromagnetic calculations within tight-binding was deemed suitable for the line-tension model.

We see a reduction in the kink-pair formation enthalpy of pure iron in tight-binding, by 0.15 eV compared to DFT, due to the smaller overall Peierls potential in both the *sd* and *d* tight-binding models. This would increase the rate of kink nucleation in kMC models, causing a higher overall dislocation velocity. We do not expect this discrepancy will significantly change the principal mechanisms observed, or results obtained, from kMC simulations.

As in Lüthi [37], carbon interactions were found to be vital in understanding how screw dislocations move in steels, due to the spontaneous reconstruction of the pure iron ground state (easy core) upon introduction of carbon. From the large binding energy of the H1 site, one would expect a

hard core with carbon in a prismatic site as the ground state configuration for pinned dislocations.

In the context of dislocation-assisted carbon migration, with sufficient contact stress, dislocations in their hard core ground state will be forced to move (say, along the  $X = \langle \bar{2}11 \rangle$  direction), which results in the hard core reconstructing to an easy core. In the limit of rapid glide, the prismatic carbon will stay in-place, becoming an E1 site. A drag force now acts to impede motion of the dislocation, due to the binding of the carbon in the E1 site. Progression of dislocation glide results in further reconstruction of the dislocation core to hard and easy states, with the original carbon being situated in H2, E6 and H3 sites, relative to the dislocation centre. Thus as the dislocation moves, there is a significant drag force acting on the dislocation, which decreases the further the dislocation moves from carbon, as one would expect. In this scenario, the kink-pair formation would increase greatly, due to this drag force. However, due to the reduced barrier for carbon migration within the vicinity of a dislocation and large average velocity in comparison to the screw dislocation, we cannot assume that carbon will stay in-place. These results suggest a dislocation-assisted carbon migration mechanism could be feasible, but the last stage of the multi-scale model, SCKMC, is necessary to verify this.

In normal operating temperatures of the bearing, one expects all dislocations to be hard cores saturated with carbon in most of the H $j$  sites, as seen in the concentration analysis. In ferrite that has just transformed, assuming a C concentration of 0.6 wt% as seen in martensite, we expect similar behaviour to the 1000 appm case as seen in figure 10.

## 16 Future work

Using the kink-pair formation enthalpies and the binding energies of carbon to screw dislocations, one can proceed with self-consistent kinetic Monte Carlo simulations of dislocation glide in an environment of carbon to understand how dislocations move carbon under applied stress, in different temperature and nominal carbon concentration regimes.

It would be of interest to pursue atomistic calculations of carbon bound to edge dislocations. Recent DFT/Eshelby theory calculations by Maugis *et al.* [38], show under *compressive* stress, carbon diffusivity is *enhanced*. Pipe diffusion along edge dislocations could therefore be an important aspect to consider in carbon transport, in addition to the higher mobility of edge dislocations in bcc iron. As such, edge dislocations could be quite important

within the mechanism of dislocation-assisted carbon migration.

Ising and Monte Carlo models of intersite carbon interactions have been performed using the results of DFT carbon-dislocation binding energies [37]. These calculations only considered the hard core, with carbon binding sites of the H1 prismatic site and a H2 site, (which they name  $P$  and  $O^{(4)}$  respectively). First neighbour C-C interactions were taken into account, both along the dislocation line and between carbon sites. Using the tight-binding calculations detailed in this report, we can easily apply and extend this analysis to consider more binding sites around the hard core, and observe stable carbon distributions around the easy core. Furthermore, we could calculate the kink-pair formation enthalpy in an environment of multiple carbons, accounting for the long-range ordering exhibited by carbon explicitly.

Analysis of carbon diffusion barriers around a dislocation are crucial to determining the regimes in which dislocation-assisted carbon migration is valid. EAM calculations by Nematollahi [28], find carbon migration energy barriers are significantly reduced around dislocations, giving rise to a "high mobility zone". Measurement of the migration barriers (and diffusion coefficient) for carbon to move to different sites around a screw dislocation has not been achieved with a quantum-mechanical interatomic force method, such as tight-binding, and could provide more accurate estimations of the average carbon velocity, critical stresses and critical temperatures above which carbon cannot catch up with dislocations—a crucial part of the theory of dislocation-assisted carbon migration. Future work will be to measure this diffusion barrier to determine if there are significant modifications to the kink-pair nucleation rate.

## 17 Conclusion

Dislocation-assisted carbon migration is thought to be a viable mechanism by which martensite decays to form DER regions—mostly composed of ferrite interspersed in a martensitic matrix—which enhances failure risk by RCF. There is dispute over where excess carbon from the martensitic matrix finds itself upon transformation to ferrite, of much lower carbon solubility. The current leading mechanism suggests carbon segregates to pre-existing carbides, yet experimental results show in the late stages of DER formation, pre-existing carbides are partially dissolved in areas of highly localized plasticity, implying segregation of carbon to dislocations. As such, a thorough investigation of carbon-dislocation interactions is vital to understanding how DER initially forms and progresses.

Atomistic calculations using tight-binding, the first stage in a multi-scale paradigm to understand dislocation-assisted carbon migration, found a Peierls potential with characteristics comparable to both EAM/DFT results.

Carbon distribution around the easy and hard cores were found to differ significantly, with the largest binding energy being found by carbon being situated in a prismatic site in the hard core. Carbon within  $3\text{\AA}$  of the easy core caused reconstruction to the hard core, with carbon in a prismatic site.

Equilibrium concentrations of carbon around the hard/easy cores at normal operating temperatures suggest that all dislocations are of hard core type with carbon situated in a H1/prismatic site, with reconstruction of all easy core dislocations to hard core, resulting in all dislocations being pinned.

If a dislocation moves under stress from the hard core-prismatic carbon ground state, a large drag force acts on the dislocation upon movement to adjacent easy and hard positions, assuming the carbon will stay in place due to its low diffusion coefficient, relative to dislocation velocity. The carbon-dislocation binding energies decrease with distance, and are in good agreement with literature. This suggests that a dislocation-assisted carbon migration mechanism is plausible, but more work needs to be done to confirm if so.

Calculations of the kink-pair formation enthalpy using a line-tension model finds a single carbon to have a surprisingly subtle effect on the kink-pair formation enthalpy. Allowing carbon to equilibrate between trap sites, we see the average kink-pair formation enthalpy decreases significantly upon stabilisation of the hard core. A self-consistent method is necessary to obtain more accurate estimates of the kink-pair formation enthalpy and average dislocation velocity.

Further work will be done to ascertain diffusion barriers around the dislocation, which have been shown to be significantly reduced from bulk values due to the presence of dislocations in DFT/EAM calculations [28]. These migration energy barriers are crucial to the solute drag mechanism.

SCkMC simulations will be used to determine dislocation dynamics in an environment of carbon.

## 18 Appendix

### 18.1 Regularisation of interaction energy in quadrupolar array

In isotropic elasticity, the elastic energy of a single dislocation dipole in an infinite lattice is given by

$$E_{\text{el}}^{\infty} = \frac{\mu b^2}{4\pi} \ln \left( \frac{r}{r_c} \right)$$

The contribution from periodic images to the correction is

$$E_{\text{img}} = E_{\text{el}}(\mathbf{a}, \mathbf{c}_i, r_c) - E_{\text{el}}^{\infty}(\mathbf{a}, r_c),$$

"Ghost" dipoles are introduced to account for the conditional convergence of the sum at  $\pm\alpha\mathbf{b}$  and  $\pm\beta\mathbf{b}$ , where  $\alpha = \beta = 0.5$ . We define  $E_{\text{dg}}(\mathbf{R})$  as the interaction energy of a ghost dislocation and a dipole at  $\mathbf{R}$  anisotropic elasticity equations as shown in [39].

Defining,

$$E_{\text{dd}}(\mathbf{R}) = \frac{\mu b^2}{2\pi} \ln \frac{|\mathbf{R}|^2}{|\mathbf{R} + \mathbf{a}| \cdot |\mathbf{R} - \mathbf{a}|},$$

we obtain,

$$E_{\text{img}} = \frac{1}{2} \sum_{\mathbf{R}} [E_{\text{dd}}(\mathbf{R}) - E_{\text{dg}}(\mathbf{R})] - \frac{1}{2} E_{\text{dg}}(\mathbf{R} = 0),$$

which can be subtracted from the total energy as given from atomistic calculations, for a regularised interaction energy.

## 18.2 Zero-point energy calculation

After relaxation of the C-dislocation system, a 3x3 Hessian matrix is constructed by taking the numerical derivative of forces observed on the carbon atom after displacement by  $\pm 0.015$  in each of the  $X$ ,  $Y$  and  $Z$  directions. The three atoms surrounding the core on the first and third layers were again fixed in  $Z$  coordinate. The zero-point energy is given by

$$E_z = \frac{1}{2} \sum_{i=1}^3 \frac{h}{2\pi} \sqrt{k_i/m_C},$$

where  $k_i$  are the eigenvalues of the Hessian and  $m_C$  is the mass of carbon.

## 18.3 Smooth mapping of sites in equilibrium line-tension model

To approximate the position of trap sites upon dislocation movement, the  $x$ -coordinate of the dislocation core position,  $P_x$ , was used to obtain the trap site positions around the core.

Focussing on one half of the the path of a dislocation between peierls valleys, the segment of a dislocation going between an easy core to hard core, one can define forward and backwards paths, a dislocation travelling from the easy core towards the hard core, and vice versa. The trap sites at the end points are well-defined: when  $P_x = P_x^{\text{easy}} = 0$ , the trap sites are exactly those found upon relaxation of the easy core, similarly, when  $P_x = P_x^{\text{hard}} = a\sqrt{2}/(2\sqrt{3}) = d$ , the trap sites are those found upon relaxation of the hard core. These positions can be seen in section 14.3.

One can define trap site mappings for these forward and backwards paths: for an easy core site to a hard core site,  $E_j^\alpha \rightarrow H_k^\beta$ , and from hard core to easy core  $H_l^\gamma \rightarrow E_m^\delta$ , where  $j, k, l, m$  denote a particular trap site position, with labels defined in section 14.3 and  $\alpha, \beta, \gamma, \delta$  are labels which denote which of the six possible sectors the site belongs to. These six sectors arise from the combination of the three-fold rotational and reflection symmetry found in the crystal—thus one need only have the trap sites for one sector and apply the appropriate rotation and/or reflection to obtain the necessary trap site position at the given endpoint. These mappings are not symmetric for the forward and backwards paths, *e.g.* are many easy core trap sites which map to the H1 site, due to its strong binding energy, as found in atomistic simulations of reconstruction, but, quite clearly, these mappings

For a given mapping, one can linearly interpolate between the two positions to give a trap site position for an intermediate dislocation core.

$$P_{j,k}^{\text{trap forward}}(P_x) = \left(1 - \frac{P_x}{d}\right) E_j^\alpha + \frac{P_x}{d} H_k^\beta,$$

$$P_{l,m}^{\text{trap backward}}(P_x) = \left(1 - \frac{P_x}{d}\right) E_m^\delta + \frac{P_x}{d} H_l^\gamma.$$

To define trap site mappings for core positions at  $P_x > d$ , one need only swap the forward for the backwards path, due to reflection symmetry about  $P_x = d$ , thus allowing for well defined trap sites for all core positions between the peierls valleys. This can be seen in the kink-pair formation of the canonical- $d$  tight-binding model in figure 25.

## 19 Bibliography

### References

- [1] M. W. Finnis, A. T. Paxton, M. Methfessel, and M. van Schilfgaarde, “Self-consistent tight-binding approximation including polarisable ions,”

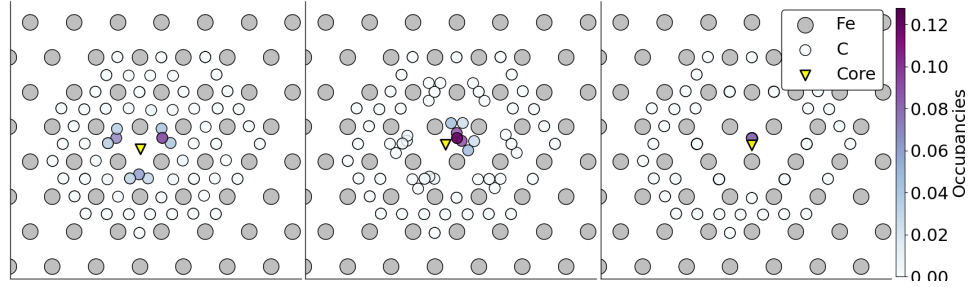


Fig. 24: Positions of trap sites around dislocation segments upon kink-pair formation at a nominal carbon concentration of 30 appm. Path only shown to the hard core to demonstrate smooth mapping of trap sites going from easy to hard core. Equilibrium occupancies shown by coloured circles.

*MRS Proceedings*, vol. 491, jan 1997.

- [2] P. Hohenberg and W. Kohn, “Inhomogeneous electron gas,” *Phys. Rev.*, vol. 136, pp. B864–B871, Nov 1964.
- [3] W. Kohn and L. J. Sham, “Self-consistent equations including exchange and correlation effects,” *Phys. Rev.*, vol. 140, pp. A1133–A1138, Nov 1965.
- [4] V. Heine, “Electronic structure from the point of view of the local atomic environment,” in *Solid State Physics*, pp. 1–127, Elsevier, 1980.
- [5] A. T. Paxton and C. Elsässer, “Analysis of a carbon dimer bound to a vacancy in iron using density functional theory and a tight binding model,” *Physical Review B*, vol. 87, June 2013.
- [6] H. Fu, E. Galindo-Nava, and P. R.-D. del Castillo, “Modelling and characterisation of stress-induced carbide precipitation in bearing steels under rolling contact fatigue,” *Acta Materialia*, vol. 128, pp. 176–187, Apr. 2017.
- [7] A. H. King and J. L. O’Brian, *Microstructural Alterations in Rolling Contact Fatigue*, pp. 74–74–15. Advances in Electron Metallography: Vol. 6, ASTM International, nil.
- [8] A. B. Jones, *Metallographic Observations of Ball Bearing Fatigue Phenomena*, pp. 35–35–18. Symposium on Testing of Bearings, ASTM International, nil.



- [9] J. J. Bush, W. L. Grube, and G. H. Robinson, “Microstructural, micro-hardness and residual stress changes due to rolling contact,” *Tribology*, vol. 3, no. 4, p. 249, 1970.
- [10] H. Swahn, P. C. Becker, and O. Vingsbo, “Martensite decay during rolling contact fatigue in ball bearings,” *Metallurgical Transactions A*, vol. 7, pp. 1099–1110, Aug. 1976.
- [11] A. P. Voskamp and E. J. Mittermeijer, “State of residual stress induced by cyclic rolling contact loading,” *Materials Science and Technology*, vol. 13, no. 5, pp. 430–438, 1997.
- [12] I. Polonsky, “On white etching band formation in rolling bearings,” *Journal of the Mechanics and Physics of Solids*, vol. 43, no. 4, pp. 637–669, 1995.
- [13] H. Fu, W. Song, E. I. Galindo-Nava, and P. E. R.-D. del Castillo, “Strain-induced martensite decay in bearing steels under rolling contact fatigue: Modelling and atomic-scale characterisation,” *Acta Materialia*, vol. 139, no. nil, pp. 163–173, 2017.
- [14] A. Warhadpande, F. Sadeghi, and R. D. Evans, “Microstructural alterations in bearing steels under rolling contact fatigue part 1—historical overview,” *Tribology Transactions*, vol. 56, pp. 349–358, May 2013.
- [15] A. Warhadpande, F. Sadeghi, and R. D. Evans, “Microstructural alterations in bearing steels under rolling contact fatigue: Part 2—diffusion-based modeling approach,” *Tribology Transactions*, vol. 57, pp. 66–76, Nov. 2013.
- [16] A. P. Voskamp, R. Österlund, P. C. Becker, and O. Vingsbo, “Gradual changes in residual stress and microstructure during contact fatigue in ball bearings,” *Metals Technology*, vol. 7, no. 1, pp. 14–21, 1980.
- [17] S. Hashemi, “Strength-hardness statistical correlation in api x65 steel,” *Materials Science and Engineering: A*, vol. 528, no. 3, pp. 1648–1655, 2011.
- [18] H. K. D. H. Bhadeshia, “Solution to the bagaryatskii and isaichev ferrite–cementite orientation relationship problem,” *Materials Science and Technology*, vol. 34, pp. 1666–1668, May 2018.

- [19] L. Ventelon, B. Lüthi, E. Clouet, L. Proville, B. Legrand, D. Rodney, and F. Willaime, “Dislocation core reconstruction induced by carbon segregation in bcc iron,” *Physical Review B*, vol. 91, June 2015.
- [20] M. Itakura, H. Kaburaki, M. Yamaguchi, and T. Okita, “The effect of hydrogen atoms on the screw dislocation mobility in bcc iron: a first-principles study,” *Acta Materialia*, vol. 61, no. 18, pp. 6857–6867, 2013.
- [21] M. Itakura, H. Kaburaki, and M. Yamaguchi, “First-principles study on the mobility of screw dislocations in bcc iron,” *Acta Materialia*, vol. 60, pp. 3698–3710, May 2012.
- [22] E. Clouet, “Screw dislocation in zirconium: An ab initio study,” *Physical Review B - Condensed Matter and Materials Physics*, vol. 86, no. 14, pp. 1–11, 2012.
- [23] V. Bulatov, *Computer Simulations of Dislocations (Oxford Series on Materials Modelling)*. Oxford University Press, dec 2006.
- [24] E. Clouet, L. Ventelon, and F. Willaime, “Dislocation core energies and core fields from first principles,” *Physical Review Letters*, vol. 102, Feb. 2009.
- [25] S. Morito, J. Nishikawa, and T. Maki, “Dislocation density within lath martensite in fe-c and fe-ni alloys,” *ISIJ International*, vol. 43, no. 9, pp. 1475–1477, 2003.
- [26] D. Rodney and L. Proville, “Stress-dependent peierls potential: Influence on kink-pair activation,” *Physical Review B*, vol. 79, Mar. 2009.
- [27] S. Makri, C. Ortner, and J. R. Kermode, “A preconditioning scheme for minimum energy path finding methods,” *The Journal of Chemical Physics*, vol. 150, p. 094109, Mar. 2019.
- [28] G. A. Nematollahi, B. Grabowski, D. Raabe, and J. Neugebauer, “Multiscale description of carbon-supersaturated ferrite in severely drawn pearlitic wires,” *Acta Materialia*, vol. 111, pp. 321–334, June 2016.
- [29] R. Veiga, M. Perez, C. Becquart, E. Clouet, and C. Domain, “Comparison of atomistic and elasticity approaches for carbon diffusion near line defects in -iron,” *Acta Materialia*, vol. 59, pp. 6963–6974, Oct. 2011.
- [30] E. Simpson, *A Tight Binding Study of Dislocations in Iron and Their Interactions with Hydrogen*. PhD thesis, King’s College London, 2019.

- [31] E. Clouet, S. Garruchet, H. Nguyen, M. Perez, and C. S. Becquart, “Dislocation interaction with c in -fe: A comparison between atomic simulations and elasticity theory,” *Acta Materialia*, vol. 56, pp. 3450–3460, Aug. 2008.
- [32] C. Becquart, J. Raulot, G. Bencteux, C. Domain, M. Perez, S. Garruchet, and H. Nguyen, “Atomistic modeling of an fe system with a small concentration of c,” *Computational Materials Science*, vol. 40, pp. 119–129, July 2007.
- [33] Y. Hanlunmyuang, P. Gordon, T. Neeraj, and D. Chrzan, “Interactions between carbon solutes and dislocations in bcc iron,” *Acta Materialia*, vol. 58, pp. 5481–5490, Sept. 2010.
- [34] W. Spitzig and A. Keh, “Orientation dependence of the strain-rate sensitivity and thermally activated flow in iron single crystals,” *Acta Metallurgica*, vol. 18, p. 1021–1033, Sep 1970.
- [35] M. Finnis, *Interatomic Forces in Condensed Matter*. Oxford University Press.
- [36] H. Yoshinaga and S. Morozumi, “The solute atmosphere round a moving dislocation and its dragging stress,” vol. 23, no. 186, pp. 1367–1385.
- [37] B. Lüthi, F. Berthier, L. Ventelon, B. Legrand, D. Rodney, and F. Willaime, “Ab initio thermodynamics of carbon segregation on dislocation cores in bcc iron,” *Modelling and Simulation in Materials Science and Engineering*, vol. 27, p. 074002, July 2019.
- [38] P. Maugis and D. Kandaskalov, “Revisiting the pressure effect on carbon migration in iron,” *Materials Letters*, vol. 270, p. 127725, July 2020.
- [39] W. Cai, V. V. Bulatov, J. Chang, J. Li, and S. Yip, “Periodic image effects in dislocation modelling,” *Philosophical Magazine*, vol. 83, pp. 539–567, Jan. 2003.

Investigating dislocation-assisted carbon migration in bcc Fe  
0.9

## References

- [1] M. W. Finnis, A. T. Paxton, M. Methfessel, and M. van Schilfgaarde, “Self-consistent tight-binding approximation including polarisable ions,” *MRS Proceedings*, vol. 491, jan 1997.
- [2] P. Hohenberg and W. Kohn, “Inhomogeneous electron gas,” *Phys. Rev.*, vol. 136, pp. B864–B871, Nov 1964.
- [3] W. Kohn and L. J. Sham, “Self-consistent equations including exchange and correlation effects,” *Phys. Rev.*, vol. 140, pp. A1133–A1138, Nov 1965.
- [4] V. Heine, “Electronic structure from the point of view of the local atomic environment,” in *Solid State Physics*, pp. 1–127, Elsevier, 1980.
- [5] A. T. Paxton and C. Elsässer, “Analysis of a carbon dimer bound to a vacancy in iron using density functional theory and a tight binding model,” *Physical Review B*, vol. 87, June 2013.
- [6] H. Fu, E. Galindo-Nava, and P. R.-D. del Castillo, “Modelling and characterisation of stress-induced carbide precipitation in bearing steels under rolling contact fatigue,” *Acta Materialia*, vol. 128, pp. 176–187, Apr. 2017.
- [7] A. H. King and J. L. O’Brian, *Microstructural Alterations in Rolling Contact Fatigue*, pp. 74–74–15. *Advances in Electron Metallography: Vol. 6*, ASTM International, nil.
- [8] A. B. Jones, *Metallographic Observations of Ball Bearing Fatigue Phenomena*, pp. 35–35–18. *Symposium on Testing of Bearings*, ASTM International, nil.
- [9] J. J. Bush, W. L. Grube, and G. H. Robinson, “Microstructural, microhardness and residual stress changes due to rolling contact,” *Tribology*, vol. 3, no. 4, p. 249, 1970.
- [10] H. Swahn, P. C. Becker, and O. Vingsbo, “Martensite decay during rolling contact fatigue in ball bearings,” *Metallurgical Transactions A*, vol. 7, pp. 1099–1110, Aug. 1976.
- [11] A. P. Voskamp and E. J. Mittermeijer, “State of residual stress induced by cyclic rolling contact loading,” *Materials Science and Technology*, vol. 13, no. 5, pp. 430–438, 1997.

- [12] I. Polonsky, “On white etching band formation in rolling bearings,” *Journal of the Mechanics and Physics of Solids*, vol. 43, no. 4, pp. 637–669, 1995.
- [13] H. Fu, W. Song, E. I. Galindo-Nava, and P. E. R.-D. del Castillo, “Strain-induced martensite decay in bearing steels under rolling contact fatigue: Modelling and atomic-scale characterisation,” *Acta Materialia*, vol. 139, no. nil, pp. 163–173, 2017.
- [14] A. Warhadpande, F. Sadeghi, and R. D. Evans, “Microstructural alterations in bearing steels under rolling contact fatigue part 1—historical overview,” *Tribology Transactions*, vol. 56, pp. 349–358, May 2013.
- [15] A. Warhadpande, F. Sadeghi, and R. D. Evans, “Microstructural alterations in bearing steels under rolling contact fatigue: Part 2—diffusion-based modeling approach,” *Tribology Transactions*, vol. 57, pp. 66–76, Nov. 2013.
- [16] A. P. Voskamp, R. Österlund, P. C. Becker, and O. Vingsbo, “Gradual changes in residual stress and microstructure during contact fatigue in ball bearings,” *Metals Technology*, vol. 7, no. 1, pp. 14–21, 1980.
- [17] S. Hashemi, “Strength-hardness statistical correlation in api x65 steel,” *Materials Science and Engineering: A*, vol. 528, no. 3, pp. 1648–1655, 2011.
- [18] H. K. D. H. Bhadeshia, “Solution to the bagaryatskii and isaichev ferrite–cementite orientation relationship problem,” *Materials Science and Technology*, vol. 34, pp. 1666–1668, May 2018.
- [19] L. Ventelon, B. Lüthi, E. Clouet, L. Proville, B. Legrand, D. Rodney, and F. Willaime, “Dislocation core reconstruction induced by carbon segregation in bcc iron,” *Physical Review B*, vol. 91, June 2015.
- [20] M. Itakura, H. Kaburaki, M. Yamaguchi, and T. Okita, “The effect of hydrogen atoms on the screw dislocation mobility in bcc iron: a first-principles study,” *Acta Materialia*, vol. 61, no. 18, pp. 6857–6867, 2013.
- [21] M. Itakura, H. Kaburaki, and M. Yamaguchi, “First-principles study on the mobility of screw dislocations in bcc iron,” *Acta Materialia*, vol. 60, pp. 3698–3710, May 2012.

- [22] E. Clouet, “Screw dislocation in zirconium: An ab initio study,” *Physical Review B - Condensed Matter and Materials Physics*, vol. 86, no. 14, pp. 1–11, 2012.
- [23] V. Bulatov, *Computer Simulations of Dislocations (Oxford Series on Materials Modelling)*. Oxford University Press, dec 2006.
- [24] E. Clouet, L. Ventelon, and F. Willaime, “Dislocation core energies and core fields from first principles,” *Physical Review Letters*, vol. 102, Feb. 2009.
- [25] S. Morito, J. Nishikawa, and T. Maki, “Dislocation density within lath martensite in fe-c and fe-ni alloys,” *ISIJ International*, vol. 43, no. 9, pp. 1475–1477, 2003.
- [26] D. Rodney and L. Proville, “Stress-dependent peierls potential: Influence on kink-pair activation,” *Physical Review B*, vol. 79, Mar. 2009.
- [27] S. Makri, C. Ortner, and J. R. Kermode, “A preconditioning scheme for minimum energy path finding methods,” *The Journal of Chemical Physics*, vol. 150, p. 094109, Mar. 2019.
- [28] G. A. Nematollahi, B. Grabowski, D. Raabe, and J. Neugebauer, “Multiscale description of carbon-supersaturated ferrite in severely drawn pearlitic wires,” *Acta Materialia*, vol. 111, pp. 321–334, June 2016.
- [29] R. Veiga, M. Perez, C. Becquart, E. Clouet, and C. Domain, “Comparison of atomistic and elasticity approaches for carbon diffusion near line defects in -iron,” *Acta Materialia*, vol. 59, pp. 6963–6974, Oct. 2011.
- [30] E. Simpson, *A Tight Binding Study of Dislocations in Iron and Their Interactions with Hydrogen*. PhD thesis, King’s College London, 2019.
- [31] E. Clouet, S. Garruchet, H. Nguyen, M. Perez, and C. S. Becquart, “Dislocation interaction with c in -fe: A comparison between atomic simulations and elasticity theory,” *Acta Materialia*, vol. 56, pp. 3450–3460, Aug. 2008.
- [32] C. Becquart, J. Raulot, G. Bencteux, C. Domain, M. Perez, S. Garruchet, and H. Nguyen, “Atomistic modeling of an fe system with a small concentration of c,” *Computational Materials Science*, vol. 40, pp. 119–129, July 2007.

- [33] Y. Hanlunmyuang, P. Gordon, T. Neeraj, and D. Chrzan, “Interactions between carbon solutes and dislocations in bcc iron,” *Acta Materialia*, vol. 58, pp. 5481–5490, Sept. 2010.
- [34] W. Spitzig and A. Keh, “Orientation dependence of the strain-rate sensitivity and thermally activated flow in iron single crystals,” *Acta Metallurgica*, vol. 18, p. 1021–1033, Sep 1970.
- [35] M. Finnis, *Interatomic Forces in Condensed Matter*. Oxford University Press.
- [36] H. Yoshinaga and S. Morozumi, “The solute atmosphere round a moving dislocation and its dragging stress,” vol. 23, no. 186, pp. 1367–1385.
- [37] B. Lüthi, F. Berthier, L. Ventelon, B. Legrand, D. Rodney, and F. Willaime, “Ab initio thermodynamics of carbon segregation on dislocation cores in bcc iron,” *Modelling and Simulation in Materials Science and Engineering*, vol. 27, p. 074002, July 2019.
- [38] P. Maugis and D. Kandaskalov, “Revisiting the pressure effect on carbon migration in iron,” *Materials Letters*, vol. 270, p. 127725, July 2020.
- [39] W. Cai, V. V. Bulatov, J. Chang, J. Li, and S. Yip, “Periodic image effects in dislocation modelling,” *Philosophical Magazine*, vol. 83, pp. 539–567, Jan. 2003.

## 20 Regularisation of interaction energy in quadrupolar array

In isotropic elasticity, the elastic energy of a single dislocation dipole in an infinite lattice is given by

$$E_{\text{el}}^{\infty} = \frac{\mu b^2}{4\pi} \ln \left( \frac{r}{r_c} \right)$$

The contribution from periodic images to the correction is

$$E_{\text{img}} = E_{\text{el}}(\mathbf{a}, \mathbf{c}_i, r_c) - E_{\text{el}}^{\infty}(\mathbf{a}, r_c),$$

"Ghost" dipoles are introduced to account for the conditional convergence of the sum at  $\pm\alpha\mathbf{b}$  and  $\pm\beta\mathbf{b}$ , where  $\alpha = \beta = 0.5$ . We define  $E_{\text{dg}}(\mathbf{R})$  as the interaction energy of a ghost dislocation and a dipole at  $\mathbf{R}$  anisotropic elasticity equations as shown in [39].



Defining,

$$E_{\text{dd}}(\mathbf{R}) = \frac{\mu b^2}{2\pi} \ln \frac{|\mathbf{R}|^2}{|\mathbf{R} + \mathbf{a}| \cdot |\mathbf{R} - \mathbf{a}|},$$

we obtain,

$$E_{\text{img}} = \frac{1}{2} \sum_{\mathbf{R}} [E_{\text{dd}}(\mathbf{R}) - E_{\text{dg}}(\mathbf{R})] - \frac{1}{2} E_{\text{dg}}(\mathbf{R} = 0),$$

which can be subtracted from the total energy as given from atomistic calculations, for a regularised interaction energy.

## 21 Zero-point energy calculation

After relaxation of the C-dislocation system, a 3x3 Hessian matrix is constructed by taking the numerical derivative of forces observed on the carbon atom after displacement by  $\pm 0.015$  in each of the  $X$ ,  $Y$  and  $Z$  directions. The three atoms surrounding the core on the first and third layers were again fixed in  $Z$  coordinate. The zero-point energy is given by

$$E_z = \frac{1}{2} \sum_{i=1}^3 \frac{h}{2\pi} \sqrt{k_i/m_C},$$

where  $k_i$  are the eigenvalues of the Hessian and  $m_C$  is the mass of carbon.

## 22 Smooth mapping of sites in equilibrium line-tension model

To approximate the position of trap sites upon dislocation movement, the  $x$ -coordinate of the dislocation core position,  $P_x$ , was used to obtain the trap site positions around the core.

Focussing on one half of the the path of a dislocation between peierls valleys, the segment of a dislocation going between an easy core to hard core, one can define forward and backwards paths, a dislocation travelling from the easy core towards the hard core, and vice versa. The trap sites at the end points are well-defined: when  $P_x = P_x^{\text{easy}} = 0$ , the trap sites are exactly those found upon relaxation of the easy core, similarly, when  $P_x = P_x^{\text{hard}} = a\sqrt{2}/(2\sqrt{3}) = d$ , the trap sites are those found upon relaxation of the hard core. These positions can be seen in section 14.3.

One can define trap site mappings for these forward and backwards paths: for an easy core site to a hard core site,  $E_j^\alpha \rightarrow H_k^\beta$ , and from hard core to easy

core  $H_l^\gamma \rightarrow E_m^\delta$ , where  $j, k, l, m$  denote a particular trap site position, with labels defined in section 14.3 and  $\alpha, \beta, \gamma, \delta$  are labels which denote which of the six possible sectors the site belongs to. These six sectors arise from the combination of the three-fold rotational and reflection symmetry found in the crystal—thus one need only have the trap sites for one sector and apply the appropriate rotation and/or reflection to obtain the necessary trap site position at the given endpoint. These mappings are not symmetric for the forward and backwards paths, *e.g.* are many easy core trap sites which map to the H1 site, due to its strong binding energy, as found in atomistic simulations of reconstruction, but, quite clearly, these mappings

For a given mapping, one can linearly interpolate between the two positions to give a trap site position for an intermediate dislocation core.

$$P_{j,k}^{\text{trap forward}}(P_x) = \left(1 - \frac{P_x}{d}\right) E_j^\alpha + \frac{P_x}{d} H_k^\beta,$$

$$P_{l,m}^{\text{trap backward}}(P_x) = \left(1 - \frac{P_x}{d}\right) E_m^\delta + \frac{P_x}{d} H_l^\gamma.$$

To define trap site mappings for core positions at  $P_x > d$ , one need only swap the forward for the backwards path, due to reflection symmetry about  $P_x = d$ , thus allowing for well defined trap sites for all core positions between the peierls valleys. This can be seen in the kink-pair formation of the canonical- $d$  tight-binding model in figure 25.

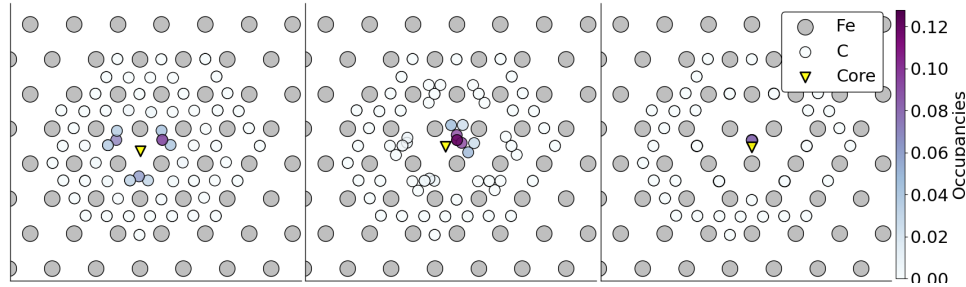


Fig. 25: Positions of trap sites around dislocation segments upon kink-pair formation at a nominal carbon concentration of 30 appm. Path only shown to the hard core to demonstrate smooth mapping of trap sites going from easy to hard core. Equilibrium occupancies shown by coloured circles.